Behavioral-transcriptomic landscape of engineered T cells targeting human cancer organoids

Authors:

Johanna F. Dekkers[1,2,3#], Maria Alieva[2,3#], Astrid Cleven[4], Farid Keramati[2], Peter Brazda[2], Heggert G. Rebel[2,3], Amber K.L. Wezenaar[2,3], Jens Puschhof[1,3], Maj-Britt Buchholz[2,3], Mario Barrera Román[2,3], Inez Johanna[4], Angelo D. Meringa[4], Domenico Fasci[4], Maarten H. Geurts[1,3], Hendrikus C.R. Ariese[2,3], Esmée J. van Vliet[2,3], Ravian L. van Ineveld[2,3], Effrosyni Karaiskaki[4], Oded Kopper[1,3], Yotam E. Bar-Ephraim[1,3], Kai Kretzschmar[1,3], Alexander M.M. Eggermont[2,5], Ellen J. Wehrens[2,3], Henk G. Stunnenberg[2], Hans Clevers[1,2,3±], Jürgen Kuball[4,6±], Zsolt Sebestyen[4±] and Anne C. Rios[2,3±]

# These authors contributed equally to this work

± These authors share senior authorship

Affiliations:

[1]Hubrecht Institute, Royal Netherlands Academy of Arts and Sciences (KNAW) and University Medical Centre (UMC) Utrecht, Utrecht, The Netherlands.

[2]Princess Máxima Center for Pediatric Oncology, Utrecht, The Netherlands.

[3]Cancer Genomics Netherlands, Oncode Institute, Utrecht, the Netherlands.

[4]Center for Translational Immunology, UMC Utrecht, Utrecht University, Utrecht, The Netherlands.

[5]UMC Utrecht, Utrecht, The Netherlands.

[6]Department of Hematology, UMC Utrecht, Utrecht University, Utrecht, The Netherlands

[*]Correspondence: a.c.rios@prinsesmaximacentrum.nl

Summary

Cellular immunotherapies are rapidly gaining clinical importance, yet predictive platforms for modeling their mode of action are lacking. Here, we developed a dynamic immuno-organoid 3D imaging-transcriptomics platform; BEHAV3D, to unravel the behavioral and underlying molecular mechanisms of solid tumor targeting. Applied to an emerging cancer metabolome-sensing immunotherapy: TEGs, we first demonstrate targeting of multiple breast cancer subtypes. Live-tracking of over 120,000 TEGs revealed a diverse behavioral landscape and identified a 'super engager' cluster with serial killing capability. Inference of single-cell behavior with transcriptomics identified the gene signature of 'super engager' killer TEGs, which contained 27 genes with no previously described T cell function. Furthermore, guided by a dynamic type 1 interferon (IFN-I) signaling module induced by high TEG-sensitive organoids, we show that IFN-I can prime resistant organoids for TEG-mediated killing. Thus, BEHAV3D characterizes behavioral-phenotypic heterogeneity of cellular immunotherapies and holds promise for improving solid tumor-targeting in a patient-specific manner.

Keywords:

BEHAV3D, multispectral time-lapse 3D imaging, behavioral classification, behavior-guided transcriptomics, patient-derived organoids (PDOs), breast cancer, T cell therapy, αβ T cells engineered to express a Vγ9/Vδ2 T cell receptor (TEGs), breast cancer, serial killing

47 **Introduction**

48 Single-cell analyses are providing unprecedented opportunities to analyze the complexity of
49 biological systems (van der Leun et al., 2020). However, they are restricted to providing a
50 snapshot of cellular processes at a given timepoint. Yet living cells are highly dynamic, and
51 their dynamic behavior shapes their function. Therefore, the development of technologies that
52 address individual cell dynamics within a population is essential for understanding cellular
53 behaviors and how these behaviors relate to function. Immune cells engineered to locate and
54 kill tumor cells represent such dynamic cell populations with an increasing clinical importance
55 (June and Sadelain, 2018). Successes of T cell therapies for hematological malignancies have
56 sparked efforts to translate such approaches to solid tumors, including breast cancer (BC), but
57 efficacy has so far been limited (Chen and Mellman, 2017). This poses a clear need for better
58 understanding the mechanism of action of cellular therapies in order to optimize treatment
59 design.

60

61 Because of challenges in identifying tumor-specific antigens for solid cancers (Schumacher et
62 al., 2019), pan-tumor therapies that recognize metabolic alterations in cancer cells are being
63 explored (Crowther et al., 2020). This includes an emerging therapy called TEGs, which are
64 peripheral blood αβ T cells engineered to express a Vγ9/Vδ2 T cell receptor (TCR), comprising
65 both $CD4^+$ and $CD8^+$ subsets (Gründer et al., 2012; Johanna et al., 2019; Marcu-Malina et al.,
66 2011; Sebestyen et al., 2019; Vyborova et al., 2020). These hybrid cells have the ability to
67 recognize cancer cells via the Vγ9/Vδ2 TCR that senses metabolic changes through the recently
68 identified ligand butyrophilin 2A1 (BTN2A1) bound to BTN3A1 (Rigau et al., 2020; Vyborova
69 et al., 2020). Yet, they maintain the high proliferation and memory capacity of conventional
70 αβ T cells (Marcu-Malina et al., 2011). TEGs are currently in clinical trials for various

leukemia (Sebestyen et al., 2019), but their potential to target solid tumors remains unknown and should be adressed in adequate preclinical models.

There is a growing interest to use organoid technology to model immunotherapy function (Bar-Ephraim et al., 2019; Cattaneo et al., 2020; Neal et al., 2018; Schnalzger et al., 2019; Dijkstra et al., 2018). Patient-derived organoids (PDOs) provide reliable *in vitro* human cancer models that recapitulate important characteristics of the original tumor specimen (Tuveson et al.), allowing for the study of patient-specifc therapy responses (Ganesh et al., 2019; Ooft et al., 2019; Tiriac et al., 2018; Vlachogiannis et al., 2018; Yao et al., 2020). In addition, imaging has proven to be a powerful approach to characterize the spatial cellular organization and tissue dynamics in these 3D structures (Dekkers et al., 2019; van Ineveld et al., *in press*; Lukonin et al., 2020; 2019; Serra et al., 2019). Here, we aim to combine organoid and 3D imaging technology for the analysis of functional single cell behavior integrated with transcriptomic profiling to decipher and manipulate the solid tumor-targeting strategy of engineered immune cells (**Video S1**).

Results

3D live-tracked TEG targeting efficacy

We devised a multispectral 3D image-based platform; BEHAV3D, to live-track efficacy and mode-of-action of cellular immunotherapy for ~60 human cancer organoid cultures simultaneously (**Figures 1A-1C; Video S1**). Multiple real-time fluorescent dyes and nanobody technology were implemented for single acquisition 4-fluorophore spectral 3D imaging of T cell populations, organoids, and dead cells, allowing us to track single TEGs, individual organoids and their death-dynamics over 24 h (**Figures 1B, 1C, and S1A-S1C**). We detected

96 a high variation of TEG-mediated killing efficacy in cultures derived from 14 BC patients
97 (**Figure 1D; Table S1**), and different targeting kinetics over time (**Figures 1E, 1F, and S1D-**
98 **S1F**), with percentages of dying PDOs ranging from near 0% (e.g. 34T) to 100% (e.g. 13T)
99 (**Figure 1F**). Pearson correlation analysis between imaging data and a commonly used cell
100 viability assay **(Figures S1G and S1H)**, or interferon gamma (IFN-γ) secretion measured by
101 ELISA **(Figures S1I and S1J)**, confirmed robustness of our imaging quantification method.
102 Among the 6 highest TEG-sensitive PDO cultures (above 50% dying organoids; **Figure 1F**),
103 we noted cultures derived from primary BC of distinct subtypes (triple negative breast cancer
104 (TNBC), human epidermal growth factor receptor 2 $(HER2)^+$, estrogen receptor $(ER)^+$, and
105 ER^+ progesterone receptor $(PR)^+HER2^+$) and from a metastasis derived from a $HER2^+$ primary
106 tumor (**Figures 1D and 1F**), supporting the potential of TEGs in targeting a broad spectrum of
107 BCs. Importantly, TEGs control the growth of PDO-derived breast tumors (TNBC primary
108 tumor and $HER2^+$ metastasis) in mouse xenograft models (**Figure 1G**), showing efficacy of
109 TEG for BC *in vivo*.
110
111 **PDO inflammatory features associate with TEG sensitivity**
112 Bulk RNA sequencing of PDOs revealed differentially expressed genes (DEGs) between the 6
113 lowest versus the 6 highest TEG-sensitive PDO cultures (**Table S2**), related to upregulated
114 cadherin signaling and steroid biosynthesis pathways in TEG-insensitive cultures, whereas
115 cytokine signaling, as well as extracellular matrix (ECM) organization, correlated with high
116 sensitivity to TEG therapy (**Figures 1H, and S1K-S1M**). The highest association was found
117 between TEG killing and type 1 interferon (IFN-I) signaling genes, including MX1, IFIT1,
118 OASL, and XAF1, which were highly expressed especially in the 2 highest TEG-sensitive PDO
119 cultures; 14T and 13T (**Figures 1H, and S1M)**. Thus, PDOs maintain tumor-specific

120 inflammatory features in culture, highlighting their utility for modeling cellular
121 immunotherapy responses in a patient-specific manner.
122
123 **TEGs display a high diversity in behavior and killing potential**
124 BEHAV3D implements single immune cell tracking in a 3D space over time and behavioral
125 classification (**Figures 1B, and 2A; Video S1**), revealing that -when exposed to PDOs- TEGs
126 could be separated into nine subpopulations with unique behavioral patterns (**Figures 2B-2D,**
127 **and S2A, S2B**). Patterns varied from inactive behaviors (*dying*, *static* and *lazy*) to active
128 motility (*slow scanner*, *medium scanner* and *super scanner*) and organoid engagement (*tickler*,
129 *engager* and *super engager*), thus demonstrating a high level of behavioral heterogeneity.
130 Having captured their behavioral single-cell landscape in this classifier (**Figures S3C-S3E)**,
131 we next predicted TEG behavior when co-cultured with PDOs that showed varying TEG
132 sensitivity (34T, 100T, 27T, 10T or 13T; **Figure 1F**), as well as an organoid culture derived
133 from normal breast tissue, which only showed minimal death when cultured with TEGs
134 (**Figure 2E**). A total of 123,296 TEGs were live-tracked to investigate how the organoid
135 (inflammatory) profile shapes T cell behavior. For each PDO culture, TEGs displayed unique
136 distributions of behavioral signatures (**Figure 2E**) and higher organoid killing associated with
137 an increase in tumor engagement (*tickler*, *engager* and *super engager*), while *static, lazy* and
138 *medium scanner* behavior decreased (**Figure 2F**). Correlation between single organoid dying
139 dynamics and TEG engagement over time revealed that organoids contacted by *super*
140 *engagers*, as compared to other organoid-engaging clusters, had the highest chance of being
141 killed (**Figures 2G, and S2F).** This indicates that effective killing by TEGs relies on prolonged
142 organoid contact, a main feature of *super engagers* (48 ± 8 min / hr; mean ± s.d.).
143
144

145 **Serial killing capability of *super engager* CD8$^+$ TEGs**

146 We next linked behaviors to population phenotypes by first differentially labeling CD4$^+$ and
147 and CD8$^+$ T cells **(Figures 3A, and S3A**). This revealed that prolonged organoid contact and
148 *super engager* behavior was a preferred feature of CD8$^+$ TEGs, whereas CD4$^+$ TEGs showed
149 a higher proportion of *lazy* cells, *slow scanners*, *medium scanners*, *super scanners*, and *ticklers*
150 (**Figures 3A-3C)** characteristic of high movement and short organoid contact (**Figure 2C**).
151 Furthermore, long-term behavior classification and back-projection of cells classified in the
152 live-tracked imaging dataset (**Figures S3B and S3C**), showed that single CD8$^+$ TEGs, once
153 engaged with an organoid, most often killed multiple cells consecutively (serial killing)
154 (**Figures 3D-3G**), a preferred feature of engineered T cells(Cazaux et al., 2019; Halle et al.,
155 2016; Weigelin et al.). In contrast, CD4$^+$ TEGs often moved away after organoid engagement
156 without killing, but occasionally targeted individual cells in different organoids (**Figures 3D-**
157 **3F, and S3D**) thereby displaying slower killing rates (**Figure 3H**). Serial killing by *super*
158 *engager* CD8$^+$ TEGs was characterized by attachment to PDOs using a defined anchor point
159 from where surrounding cells were killed via long protrusions, intercalating between epithelial
160 cells and extending their initial size up to 5 times (**Figures 3E, and S3E and S3F**).
161 Remarkably, single CD8$^+$ TEGs were able to kill entire organoids (up to 18 cells in 11 hrs;
162 **Figures 3E and 3G; Video S1**). This extent of serial killing and morphological plasticity of
163 *super engager* CD8$^+$ TEGs was uniquely revealed by the high spatiotemporal resolution
164 character of BEHAV3D.

165

166 **NCAM1 associates with *super engager* behavior**

167 Through single cell RNA sequencing (scRNAseq), we observed differential expression of
168 NCAM1 in CD8$^+$ TEGs (**Figures 3I**, **S3G and S3H; Table S3**). Although linked to
169 cytotoxicity in both αβ and γδ T cells(Van Acker et al., 2017), this surface marker has not been

170 examined in the context of cellular immunotherapy. We confirmed potent effector function
171 related to NCAM1 expression, by showing that NCAM1^{+}CD8^{+} TEGs had a higher capacity to
172 kill 13T organoids compared to NCAM1^{-}CD8^{+} TEGs (**Figure 3J**). To identify behavioral
173 mechanisms underlying this high killing potential, we pre-labeled CD8^{+} TEGs with NCAM1
174 nanobodies (**Figure 3K)**, to directly compare NCAM1-positive and -negative populations
175 within the same environment. NCAM1^{+}CD8^{+} TEGs showed reduced *dying* and *static* behavior
176 (**Figures 3L and 3M, and S3I**), supporting a higher *in vitro* persistence. Strikingly,
177 NCAM1^{+}CD8^{+} TEGs additionally showed a significant increase in *super engager* behavior
178 compared to NCAM1^{-}CD8^{+} TEGs (**Figure 3L and 3M**). Thus, surface marker expression can
179 be linked to engineered T cell behavior, offering the opportunity to enrich for potent effector
180 behaviors.
181
182 **Behavioral-transcriptomic profiling of TEGs**
183 To generate insight into the transcriptional programs that underlie tumor-targeting dynamics
184 revealed by BEHAV3D, we next performed single cell transcriptomic profiling of TEG
185 populations enriched for different behavioral signatures, including a TEG population
186 containing > 90% *super engagers* (**Figures 4A and 4B, and S4A; Video S1**). For each main
187 TEG subset, effector CD8^{+} (CD8^{+eff}), effector CD4^{+} (CD4^{+eff}) and memory CD4^{+} (CD4^{+mem}),
188 profound transcriptional changes were observed upon 6 h co-culture with highly targeted 13T
189 organoids, as compared to baseline (*no target control*) (**Figures 4C-4E**), showing that dynamic
190 interplay with PDOs shapes the TEG transcriptomic profile. Behavioral probability mapping
191 inferred from pseudotemporal ordering (**Figure S4B**) of the sequenced TEG populations
192 (**Figure 4F**), revealed dynamic transcriptional programs that were highly conserved between
193 CD8^{+eff}, CD4^{+eff}, and CD4^{+mem} TEGs (**Figure 4G**; Gene cluster (CL)1-3; 85% of genes; **Table**
194 **S4**). These programs included genes to be down- (CL1) or up-regulated (CL3) by

195 environmental stimuli or engagement to PDOs, as well as genes transiently expressed (CL2)
196 along the pseudotime trajectory (**Figure 4G;** GO terms per CL in **Figure S4C**). This
197 differential dynamic expression matched with known gene function, confirming robust
198 ordering of TEGs, as shown by genes related to the CD3 signaling complex (LCK, SOS1,
199 CD3E, CD3G; CL1; GO term 'T cell activation'), known to be down-regulated upon T cell
200 activation(Liu et al., 2000) in CL1 (**Figure 4H)**. NF-kB signaling, critical for tumor
201 control(Barnes et al., 2015), and effector molecules including FASLG, IFNG, GZMB, TNF
202 were found in CL3, with NF-kB signalling induced by environmental stimuli reaching
203 maximum expression upon prolonged PDO-engagement, while the effector molecules
204 appeared upon engagement (**Figure 4I**). In addition, CL3 contained genes related to rRNA
205 processing that only increased upon prolonged engagement with organoids (**Figure 4H**),
206 consistent with accelerated protein production in T cells following TCR engagement(Asmal et
207 al., 2003; Tan et al., 2017). Finally, CL2 contained early activation markers CD69 and EGR1
208 with peak expression upon short organoid engagement, in line with IL-2 (CL3), known to be
209 induced by EGR1(Collins et al., 2006), upregulated towards the end of the trajectory (**Figure**
210 **4I**). Thus, through our behavior-guided transcriptomics approach we robustly identified
211 dynamic gene orchestration of TEG during tumor targeting.
212
213 **Gene signature related to (serial) killing *super engager* TEGs**
214 Of gene sets regulated in a TEG subset-specific manner (CL4-8; 15% of genes), CL7 contained
215 genes mainly induced upon prolonged organoid engagement, including cytotoxic genes (e.g.
216 PRF1, CRTAM, XCL1) (**Figures 4H and 4I;** GO: 'Regulation of cell killing'). This cluster of
217 genes was specifically induced in *super engager* $CD8^{+eff}$, and to a lesser extent in $CD4^{+eff}$
218 TEGs, and almost absent in $CD4^{+mem}$ TEGs (**Figure 4J**), associating this gene cluster with
219 potent (serial) killing T cells (**Figures 3D-3G**). Analysis of TEGs derived from a different

220 healthy donor and co-cultured with another PDO culture (10T), confirmed that 61 out of the
221 83 genes of CL7 represent a conserved 'killer' gene signature (**Table S5**). Of these, we
222 identified 20 genes related to T cell activation and cytotoxicity and 14 genes related to other T
223 cell functions (**Figures 4K, and S4D**). However, importantly, we found 27 genes with no
224 previously described T cell function (**Figures 4K, and S4D**). Overall, half of all conserved
225 signature genes (31/61) and 17 out of the 27 novel genes were related to morphological
226 plasticity processes, such as motility, cytoskeleton remodeling and adhesion (**Figure S4D**).
227 Given that morphological plasticity is a key determinant of cell migration, many of the novel
228 genes were found to have a role in promoting tumor cell migration and invasion, including
229 ECM production and mesenchymal state induction (HEG1, BZW2, DCAF13, SQLE, PKIA).
230 For some of these genes, such as CCT3 or AFAP1L2, the mechanism promoting migration is
231 yet undescribed. In line with the prolonged organoid engagement behavioral feature of *super*
232 *engager* TEGs (**Figure 2C**), we also found various genes related to cell adhesion, such as
233 NCEH1, BYSL or EMP1. Finally, some genes had an additional function related to neurite
234 outgrowth and dendritic pruning (SERPINE2, CHD4, NRTK1), potentially matching the long
235 protrusion that were observed to occur in these serial killing TEGs **(Figures 3E, and Figure**
236 **S3E and S3F; Video S1).** Thus, behavioral transcriptomics identified a specific gene signature
237 induced in (serial) killing *super engager* TEGs.
238
239 **PDOs shape the dynamic gene signature of TEG during tumor targeting**
240 To further explore our behavioral-guided transcriptomics approach, we next compared
241 behavior-enriched TEG populations co-cultured between either highly sensitive 13T or
242 intermediately targeted 10T PDOs. Distinct UMAP embedding of different TEG populations
243 (**Figure 5A**) indicated that the patient-specific organoid exposure influences the dynamic TEG
244 transcriptional profile. 41% or 61% of upregulated genes by environmental stimuli or upon

245 prolonged PDO engagement in *super engagers*, respectively, were common between 10T- and
246 13T-co-cultured TEGs (**Figures 5B**, **and S5A and S5B**; **Table S6)**. Common *super engager*-
247 related gene signatures included rRNA processing, NF-kB signaling and cytokine signaling
248 (**Figure S5B**), and matched CL3 gene signatures (**Figure S4C**). However, 10T-co-cultured
249 TEGs were characterized by induction of high cytokine expression upon prolonged PDO
250 engagement, including TNF, IFNG and IL2, whereas IFN-I signaling genes were uniquely
251 induced in TEGs co-cultured with highly sensitive 13T (**Figures 5C, and S5C**).
252
253 **IFN-β primes PDOs for TEG mediated killing**
254 IFN-I signaling plays fundamental roles in anti-tumor immunity, yet with diverse and
255 sometimes opposing functions reported for both tumor and immune cells, thereby making it
256 difficult to fully comprehend and therapeutically exploit these effects(Boukhaled et al., 2021).
257 IFN-I signaling was detected in 13T organoids (**Figure S1M**), which most prominently
258 displayed increased RNA levels of the upstream mediator IFN-β, but not IFN-α, among our
259 collection of PDOs (**Figure 5D)**. Secretion of IFN-β was confirmed by Luminex (**Figure S5D**),
260 implying that IFN-β was the main mediator of IFN-I signaling observed in 13T. Interestingly,
261 peak induction of IFN-I signaling in 13T-co-cultured TEGs was detected in non-organoid-
262 engaging TEGs (from *static* to *super scanner* behavior), in line with a secreted source of IFN-
263 β, while the pathway was shut down in *super engager* TEGs, suggesting a limited role of IFN-
264 I signaling in direct killing behavior (**Figures 4F-4H**). Adding recombinant IFN-β to co-
265 cultures of TEGs with various PDOs that showed low to medium sensitivity to TEG therapy
266 (100T, 34T, 27T and 10T) indeed did not affect TEG targeting efficacy (**Figure 5E**). However,
267 34T, 27T and 10T organoids pre-treated with IFN-β showed increased TEG-mediated killing,
268 while IFN-β treatment did not impact organoid viability by itself (**Figures 5F and 5G**). These
269 data support that IFN-β has limited impact on the killing capacity of *super engager* TEGs,

270 confirming that dynamic IFN-I signaling is mainly associating with *static* to *scanner* behavior.
271 Importantly however, IFN-I signaling increases the sensitivity of organoids to TEG therapy.
272 Thus, behavior-guided TEG transcriptomics in relation to the type of organoid exposure reveals
273 IFN-β to prime PDOs for targeting by TEGs. This illustrates the potential of the BEHAV3D to
274 better understand and guide combinatory treatment approaches in a patient-specific manner.
275
276

Discussion

Here, we provide an organoid-based 3D imaging-transcriptomic platform; BEHAV3D, for understanding the mode-of-action of cellular anti-cancer immunotherapies in a patient-specific manner. Using this pipeline, we report on the broad targeting potential of TEGs for breast cancer, poorly permissive to current immunotherapies (Esteva et al., 2019). In addition, by behavior-guided transcriptomics we have generated, to our knowledge, the first molecular map underlying the behavioral landscape of immune cells targeted to solid tumors. By exploiting these results, we were able to design an optimal sequence of IFN-I and TEG combination therapy to boost TEG organoid targeting.

Different from recent studies that have mapped the activation trajectories of murine immune cells during viral infection (Abbas et al., 2020), or human immune cells in normal physiology or cancer (Szabo et al., 2019), we here reconstructed activation trajectories for engineered T cells and uniquely exploited dynamic imaging data revealing their single-cell behavior. This allowed us to dissect gene programs induced by environmental stimuli, versus induction by short or prolonged tumor engagement, and thereby identify the gene signature of TEGs that (serially) killed tumor cells. This signature includes genes not previously linked to T cell function, thereby providing novel opportunities to potentially engineer next generation T cells with potent serial killing capability. Furthermore, multiple genes in this signature are associated with morphological plasticity. Such plasticity may underlie the remarkable cellular extensions of serial-killing TEGs, as observed in our 3D imaging data. Using these protrusions, TEGs intercalate~~d~~ between tumor cells while sequentially killing multiple tumor cells in the PDO, suggesting that morphological plasticity may be an important attribute in the targeting of solid tumors.

300 Type 1 IFNs have been described to be beneficial for the control of tumor growth,
301 including in breast cancer, either by exerting direct antitumor effects (Dunn et al., 2005), or by
302 improving the response to therapies, such as chemotherapy and checkpoint inhibition (Borden,
303 2019; Sistigu et al., 2014). Yet, opposite roles in inducing treatment resistance have been
304 described as well (Benci et al., 2016; Boukhaled et al., 2021; Jacquelot et al., 2019). By using
305 defined immune-organoid co-cultures, we have shown that an IFN-I signature intrinsic to
306 tumor cells associates with TEG sensitivity, and that IFN-β primes tumor cells for more
307 efficient targeting, rather than directly affecting TEG killing behavior. Thus, our data support
308 the clinical use of IFN-I in combination with TEGs and possibly other cellular
309 immunotherapies.

310 Adding to patient-specific drug responses observed in PDOs biobanks (Ganesh et al.,
311 2019; Jacob et al., 2020; Ooft et al., 2019; Tiriac et al., 2018; Vlachogiannis et al., 2018; Yao
312 et al., 2020), we show that not only killing efficacy, but also the underlying behavioral and
313 molecular mechanisms of cellular immunotherapy differ between different PDO cultures. We
314 even detected differences in killing dynamics between individual organoids belonging to the
315 same PDO culture. This demonstrates that our platform captures the inter- and intra-patient
316 heterogeneity, a major obstacle for treating solid tumors (Yamamoto et al., 2019). It is
317 intriguing that gene signatures induced in TEGs upon organoid engagement were partly
318 dictated by the type of PDO. In addition, the extent of IFN-β pre-treatment outcome on tumor
319 targeting differed between PDOs, with the highly resistant culture 100T remaining
320 unresponsive, whereas 34T displayed the highest (4-fold) increase in targeting. Together, these
321 findings warrant caution regarding generalizing the outcome of immuno-oncology studies that
322 use a single tumor model, and further supports the value of human organoid technology for
323 development of personalized therapies.

Altogether, BEHAV3D combines organoid, imaging and sequencing technologies to offer a comprehensive platform that integrates multiple single-cell readouts, including tumor death dynamics, single-cell behavior and underlying transcriptomic profiling (**Video S1**). BEHAV3D may thus contribute to the efforts aimed at enhancing the efficacy of solid tumor-targeting by cellular therapies.

331 **Methods**

332

333 **Human material**

334 All human PDO samples were retrieved from a biobank through the Hubrecht Organoid
335 Technology (HUB, www.hub4organoids.nl). Authorizations were obtained by the medical
336 ethical committee of UMC Utrecht (METC UMCU) at request of the HUB in order to ensure
337 compliance with the Dutch medical research involving human subjects' act. The normal
338 organoids were generated from milk obtained via the Moedermelkbank Amsterdam
339 (Amsterdam UMC). Informed consent was obtained from all donors.

340

341 **Animal material**

342 NOD.Cg-PrkdcscidIl2rgtm1Wjl/SzJ (NSG) mice purchased from Charles River Laboratories
343 (France). Experiments were conducted in accordance with Institutional Guidelines under
344 acquired permission from the local Ethical Committee and as per current Dutch laws on Animal
345 Experimentation. Mice were housed in sterile conditions using an individually ventilated cage
346 (IVC) system and fed with sterile food and water. Irradiated mice were given sterile water with
347 antibiotic ciproxin for the duration of the experiment. Mice were randomized with equal
348 distribution by age and initial weight measured on day 0 and divided into 10–15 mice per
349 group.

350

351 **Organoid culture**

352 Organoids were seeded in basement membrane extract (BME; Cultrex) in uncoated 12-well
353 plates (Greiner Bio-one) and cultured as described previously(Dekkers et al., 2021; Sachs et
354 al., 2017). Briefly, Advanced DMEM/F12 was supplemented with penicillin/streptomycin
355 (pen/strep), 10 mM HEPES, Glutamax (adDMEM/F12+++), 1 x B27 (all from Thermo Fisher),

356 1.25 mM N-acetyl-L-cysteine (Sigma-Aldrich), 10 mM Nicotinamide (Sigma-Aldrich), 5 µM
357 Y-27632 (Abmole), 5 nM Heregulin β-1 (Peprotech), 500 nM A83-01 (Tocris), 5 ng/ml EGF
358 (Peprotech), 20 ng/ml FGF-10 (Peprotech), 10% Noggin-conditioned medium (NCM)
359 (Cattaneo et al., 2020), 10% Rspo1-conditioned medium (RCM) (Broutier et al., 2016), and
360 0.1 mg/ml primocin (Thermo Fisher), and in addition with 1 µM SB202190 (Sigma-Aldrich)
361 and 5 ng/ml FGF-7 (Peprotech) for PDO propagation ('Type 1' culture medium(Dekkers et al.,
362 2021)), or with 20% Wnt3a-conditioned medium (WCM) (Broutier et al., 2016), 0.5 µg/ml
363 hydrocortisone (Sigma-Aldrich), 100 µM β-estradiol (Sigma-Aldrich) and 10 mM forskolin
364 (Sigma-Aldrich) for normal organoid propagation ('Type 2' culture medium (Dekkers et al.,
365 2021)). Culture medium was refreshed every 2–3 days and organoids were passaged 1:2–1:6
366 every 7–21 days using TrypLE Express (Thermo Fisher). For co-culturing, organoids of a 5–
367 12-day old culture (depending on PDO growth speed) were recovered from the BME by
368 resuspension in TrypLE Express and collected adDMEM/F12+++. The organoid suspension
369 was filtered through a 70 µm strainer (Greiner) to remove large organoids and pelleted before
370 co-culturing. Organoids of passage 5 to 30 after cell isolation were used.
371
372 **Cell lines**
373 Daudi (Gründer et al., 2012), HL60(Marcu-Malina et al., 2011) and Phoenix-Ampho cell lines
374 were obtained from ATCC (authenticated by short tandem repeat
375 profiling/karyotyping/isoenzyme analysis). Daudi and HL60 cells were cultured in RPMI
376 media supplemented with 10% fetal calf serum (FCS) and 1% pen/strep (all from Thermo
377 Fisher). Phoenix-Ampho cells were cultured in DMEM medium (Thermo Fisher)
378 supplemented with 10% FCS and 1% pen/strep. All cells were passaged for a maximum of 2
379 months, after which new seed stocks were thawed for experimental use. Furthermore, all cell
380 lines were routinely verified by growth rate, morphology, and/or flow cytometry and tested

381 negative for mycoplasma using MycoAlert Mycoplasma Kit. Peripheral blood mononuclear
382 cells (PBMCs) were obtained from Sanquin Blood bank (Amsterdam, The Netherlands) and
383 isolated using Ficoll gradient centrifugation methods from buffy coats.
384
385 **Retroviral transduction of T cells**
386 TEG001 (T cells engineered to express a highly tumor-reactive Vγ9Vδ2 TCR) (Gründer et al.,
387 2012; Straetemans et al., 2015; 2018), LM1s (mock T cells engineered to express a mutant
388 Vγ9/Vδ2 TCR with abrogated function) (Marcu-Malina et al., 2011), and TEG011 (mock T
389 cells engineered to express HLA-A*24:02-restricted Vγ5/Vδ1 TCR; used as control for *in vivo*
390 studies) (Kierkels et al., 2019; Scheper et al., 2013), were produced as previously described
391 (Marcu-Malina et al., 2011). Briefly, packaging cells (Phoenix-Ampho) were transfected with
392 helper constructs gag-pol (pHIT60), env (pCOLT-GALV) and pMP71 retroviral vectors
393 containing both Vγ9/Vδ2 TCR chains separated by a ribosomal skipping T2A sequence, using
394 FugeneHD reagent (Promega). Human PBMCs from healthy donors were pre-activated with
395 anti CD3 (30 ng/mL; Orthoclone OKT3; Janssen-Cilag) and IL-2 (50 IU/mL; Proleukin,
396 Novartis) and subsequently transduced twice with viral supernatant within 48 hrs in the
397 presence of 50 IU/mL IL-2 and 6 mg/mL polybrene (Sigma-Aldrich). TCR-transduced T cells
398 were expanded by stimulation with anti-CD3/CD28 Dynabeads (500,000 beads/10^6 cells; Life
399 Technologies) and IL-2 (50 IU/mL). Thereafter, TCR-transduced T cells were depleted of the
400 non-engineered T cells.
401
402 **Depletion of non-engineered T cells**
403 Depletion of non-engineered T cells was performed as previously described (Marcu-Malina et
404 al., 2011). In short, αβ T cells were transduced with pMP71: γ-T2A-δ and incubated with a
405 biotin-labelled anti-αβ TCR antibody (clone BW242/412; Miltenyi Biotec) followed by

406 incubation with an anti-biotin antibody coupled to magnetic beads (anti-biotin MicroBeads;
407 Miltenyi Biotec). Next, the cell suspension was applied onto an LD column and αβ TCR-
408 positive (αβ TCR^+) T cells were depleted by Magnetic-Activated Cell Sorting (MACS)
409 according to the manufacture's protocol (Miltenyi Biotec).
410
411 **Separation of $CD4^+$ and $CD8^+$ subsets of TEGs**
412 In order to separate $CD4^+$ and $CD8^+$ TEGs and LM1s, we performed positive selection using
413 either CD4 or CD8 Microbeads (Miltenyi Biotech) following manufacturer's instructions.
414 After incubation with magnetic microbeads cells were applied to LS columns and $CD4^+$ or
415 $CD8^+$ TEGs or LM1s were selected by MACS. After MACS selection procedure, both
416 Vγ9/Vδ2 TCR^+ $CD4^+$ or Vγ9/Vδ2 TCR^+ $CD8^+$ subsets of TEGs were separately expanded by
417 using a rapid expansion protocol (REP) (Marcu-Malina et al., 2011) where TEGs were cultured
418 in 'TEG culture medium' (RPMI-Glutamax supplemented with 2,5 – 10 % human serum
419 (Sanquin), 1% pen/strep and 0.5M beta-2- mercaptoethanol) on a feeder cell mixture
420 composing of irradiated allogenic PBMCs, Daudi and LCL-TM in the presence of IL2 (50
421 U/ml; Novartis Pharma), IL15 (5 ng/ml; R&D Systems) and PHA-L (1 μg/ml; Sigma-Aldrich).
422 TEGs were stimulated biweekly by using the REP protocol. In order to monitor the purity of
423 $CD4^+$ and $CD8^+$ TEGs, cells were analyzed by flow cytometry weekly prior to functional
424 assays by using anti-pan γδ TCR-PE (Beckman Coulter), anti- αβTCR-FITC (eBioscience),
425 anti-CD8-PerCP-Cy5.5 (Biolegend) and anti-CD4-APC (Biolegend) antibodies. TEGs with a
426 purity lower than 90% were re-selected as described above. TEGs were used for co-culture
427 assays 4 – 5 days after the last IL2/IL15/PHA-L stimulation.
428
429
430

431 **Sorting of NCAM1$^{-/+}$ TEGs**

432 CD8^{+} TEGs were harvested at day 8-10 of their REP cycle, stained in flow cytometry (FC)
433 buffer (2% fetal bovine serum, 1x PBS) with Hilyte-488-conjugated NCAM1 nanobodies
434 (1:400; QVQ) and LIVE/DEAD Fixable Near-IR Dead Cell Stain (1:1000; ThermoFisher) for
435 30 minutes at 4˚C and consecutively sorted using a SONY SH800S or a FACS Aria Cell Sorter
436 (BD Biosciences) into NCAM1^{-} and NCAM^{+} populations. Cells were rested for 16 h in 'TEG
437 culture medium' and then used for co-culture.

438

439 **Live cell imaging of TEG and organoid co-cultures**

440 LM1s or TEGs (20,000) were co-cultured with normal organoids, PDOs or control cell lines
441 (Daudi or HL-60) in an effector to tumor cell (E:T) ratio of 1:3 or 1:25 (for **Figures 3D-3F**).
442 CD4^{+} and CD8^{+} TEGs were mixed in a 1:1 ratio just before plating. Cells were incubated in
443 96-well glass-bottom SensoPlates (Greiner) in 200 µl 'co-culture medium': 50% 'Type 1'
444 organoid culture medium, 50% 'TEG assay medium' (RPMI-Glutamax supplemented with
445 10% FCS and 1% pen/strep), 2.5% BME and pamidronate for the accumulation of the
446 phosphoantigen IPP to stimulate tumor cell recognition(Marcu-Malina et al., 2011) (1:2000).
447 'Co-culture medium' was supplemented with both NucRed™ Dead 647 (2 drops per ml;
448 Thermo Fisher) and TO-PRO-3 (1:3000; Thermo Fisher) for fluorescent labelling of living and
449 dead cells ('Imaging medium'). Combination of NucRed™ Dead 647 and TO-PRO-3 light up
450 dead cell when excited with the 633 nm laser, and living cells when excited with the 561 nm
451 laser (**Figures S1A and S1B**). Both were combined to achieve the most optimal fluorescent
452 intensity ratio between dead and living cells for live cell imaging. Prior to co-culturing, TEGs
453 were incubated with eBioscience™ Cell Proliferation Dye eFluor™ 450 (referred to as eFluor-
454 450; 1:4000; Thermo Fisher) in PBS for 10 min at 37 °C to fluorescently label all TEGs. When
455 CD4^{+} and CD8^{+}TEGs were simultaneously imaged, eFluor-450, as well as Calcein AM

456 (1:4000; Thermo Fisher) were used to label the different TEG subsets in PBS for 10 min at 37
457 °C. For NCAM1 pre-labeling experiments, a combination of eFluor-450 (1:4000; Thermo
458 Fisher) and Hilyte-488-conjugated NCAM1 nanobodies (1:400; QVQ) was used to label $CD8^+$
459 TEGs in PBS for 20 min at 37 °C prior to co-culturing. To prevent evaporation while imaging,
460 200 µl PBS was added to the wells surrounding the co-culture wells. The plate was placed in a
461 LSM880 (Zeiss) microscope containing an incubation chamber (37 °C; 5% CO_2) and incubated
462 for 30 min to ensure settling of TEGs and organoids at the bottom of the well. The plate was
463 imaged for up to 24 hrs with a Plan-Apochromat 20 x/0.8 NA dry objective with the following
464 settings: online fingerprinting mode, bidirectional scanning, optimal Z-stack step size, Z-stack
465 of 60 µm in total and time series with a 30 min (up to 60 conditions simultaneously; resolution
466 512 x 512) or 2 min interval (up to 4 or 10 conditions simultaneously; resolution 512 x 512 and
467 200 x 200 respectively). To minimize photobleaching of NCAM1-pre-labeled TEGs, the 488
468 nm laser was only activated 1 Z-stack each hr within the first hrs of imaging. Directly after
469 imaging, the production of IFN-γ in the supernatant was quantitated using an ELISA-ready-
470 go! Kit (eBioscience) and cell pellets were used to measure organoid viability using a CellTiter-
471 Glo® Luminescent Cell Viability Assay (Promega).
472
473 **IFN-β stimulations**
474 PDOs were harvested as described above and incubated in 96-well round bottom culture plates
475 (Thermo Fisher) in 100 µl 'Type 1' organoid culture medium, supplemented with 2.5% BME,
476 with or without the presence of 100 pg/ml recombinant human IFN-β (Peprotech). After 24 h
477 incubation (37 °C; 5% CO_2), TEGs or LM1s were added to either IFN-β-preincubated or
478 unstimulated organoids (E:T ratio of 1:3) in 100 µl 'TEG assay medium', supplemented with
479 2.5% BME and pamidronate (1:1000), with or without the presence of 100 pg/ml recombinant
480 human IFN-β (Peprotech). Medium without T cells was added for 'organoid only' controls.

481 After 16 h incubation (37 °C; 5% CO_2), plates were used to measure organoid viability using
482 a CellTiter-Glo® Luminescent Cell Viability Assay (Promega).
483
484 ***In vivo* targeting by TEGs**
485 Adult female NSG mice (15-16 weeks old) received sub-lethal total body irradiation (1,75 Gy)
486 and subcutaneous implantation of an β-estradiol pellet (Innovative Research of America) on
487 Day -1. On day 0, PDOs ($1x10^6$ 13T organoid cells in 100 µl BME per mouse) were prepared
488 as described previously (Dekkers et al., 2021) for subcutaneous injection on the right flank on
489 Day 0, and received 2 injections of 10^7 TEGs or TEG011 mock cells on day 1 and 6 in
490 pamidronate (10 mg/kg body weight) as previously reported(Johanna et al., 2019). On day 1,
491 together with the first T cell injection, all mice also received $0.6x10^6$ IU of IL-2 (Proleukin;
492 Novartis) in IFA subcutaneously. Tumor volume was measured once a week using digital
493 caliper and was calculated by the following formula: 0.4 x (length x width x width). Mice were
494 monitored at least twice a week for weight loss and clinical appearance scoring (scoring
495 parameter included hunched appearance, activity, fur texture, piloerection,
496 respiratory/breathing problem). Humane endpoint (HEP) was reached when mice experienced
497 a 20% weight loss from the initial weight, tumor volume reached 2 cm^3, or when clinical
498 appearance score of 2 was reached for individual parameter or an overall score of 4.
499
500 **Image processing**
501 For 3D visualization, cell segmentation and extraction of statistics, time-lapse movies were
502 processed with Imaris (Oxford Instruments), versions 9.2 to 9.5. The *Channel Arithmetics*
503 Xtension was used for creating new channels to specifically identify organoids (live and dead)
504 and eFluor-450-labeled or calcein AM-labeled TEGs (live and dead) and exclude cell debris.
505 The Surface and ImarisTrack modules were used for object detection and automated tracking

506 of both TEGs (autoregressive motion) and organoids ('connected components' or no tracking).
507 The *Distance Transformation* Xtension was used to measure the distance between TEGs and
508 organoids and thresholds for defining organoid–T cell interactions were visually determined.
509 For tracked TEGs, time-lapse data containing the coordinates of each cell, the values of cell
510 speed, mean square displacement, distance to organoids and dead cell dye channel intensity
511 were exported. For experiments with NCAM1 pre-labelling, the mean intensities of the
512 NCAM1 channel per T cell were exported. For tracked organoids, time-lapse data containing
513 the coordinates of each organoid, the surface area, volume and mean dead cell dye channel
514 intensity were exported.
515
516 **Imaging and sequencing data processing**
517 Analysis of imaging and sequencing data was performed using R Studio version 4.0.2, as well
518 as the following R packages: DESeq2, devtools, dplyr, dtwclust, eulerr, gganimate, ggplot2,
519 ggpubr, ggrepel, gridExtra, hypergeo, kmodR, lme4, lmerTest, MESS, nlme, openxlsx,
520 parallel, patternplot, pheatmap, plotly, plyr, png, purr, RColorBrewer, readxl, reshape2, rgeos,
521 scales, Seurat, sp, spatstat, stats, tidyr, tidyverse, umap, VennDiagram, viridis, xlsx, zoo.
522
523 **PDOs killing dynamics**
524 To quantify cell death dynamics of PDO cultures, > 5000 single organoids were analyzed at
525 each time-point (48 time-points total). The mean dead cell dye intensity within single organoid
526 surfaces, and values were rescaled to a range between 0 and 100 per experiment to normalize
527 for variation in the absolute dead cell dye intensity. Per time point, organoids were classified
528 as 'dying' when the mean dead cell dye intensity was above 7.
529
530

531 **T cell dynamics analysis and multivariate time series clustering**

532 For the analysis of TEG behavior overtime, the following parameters were used: T cell death,
533 contact with organoids, speed, square displacement and interaction with other T cells.
534 Interactions between TEGs were measured by computing the distance to the nearest neighbor
535 for each cell. To only include active interactions between TEGs that were not engaged to
536 organoids, we considered cells whose mean speed for the last 20 minutes fell within the 3rd
537 quartile. A threshold for interacting T cells was defined as 10 µm between cell centroids and
538 confirmed by visual inspection of imaging data. For each TEG time series, linear interpolation
539 was used to estimate the values in few cases of missing time points. To compare time series
540 independently of their length, cell tracks were cut to a length of 3.3 hrs. For each experimental
541 replicate, the values of each of the numeric variables were converted to z-scores. To enhance
542 the most discrepant values, only the 3rd quartile range values were kept, while the rest was
543 converted to the minimum values. Finally, each numeric variable was scaled to a range between
544 0 and 1 and normalized to the mean of the 0.99 quantile (per experimental replicate). For binary
545 variables (TEG-TEG or TEG-organoid interactions), the values were labelled as 1 or 0 for
546 interaction or no-interaction terms. Similarity between distinct cell tracks was measured using
547 a strategy that allows for best alignment between time-series, previously applied for mitotic
548 kinetics (Cai et al., 2018) or temporal module dynamics comparisons (Schafer et al., 2019). A
549 cross-distance matrix based on the multivariate time-series data was computed using the
550 dynamic time warping algorithm from the package "dtwclust". To visualize distinct cell
551 behaviors in 2 dimensions, dimensionality reduction on the multidimensional feature count
552 table was performed by Uniform Manifold Approximation and Projection method ("umap"
553 package) (Ali et al.; Becht et al., 2018). Clustering was performed using the k-means clustering
554 algorithm with outlier detection. The identity of each cluster was defined by the mean time-
555 series values of the different parameters (speed, square displacement, organoid contact, T cell

556 interactions, cell death) within each cluster (**Figure 2C**). To confirm the identity of each
557 cluster, T cell cluster assignments were back-projected to visualize the surfaces and tracks of
558 particular T cell populations in the imaging dataset (**Figures 2A, S2A and S2B, and S3B**). A
559 combination of datasets with distinct behavioral characteristics was used to construct a global
560 TEG behavior atlas using the described methodology (**Figure 2B**).
561
562 **Cell behavior classification using a Random Forest classifier**
563 For standardized integration of new experiments, we used a random forest classification
564 approach (Breiman, L., 2001) in order to relate cell behavior to the nine behavioral signatures
565 that we found in our global TEG behavior atlas (**Figure 2B**). To allow for inclusion of
566 experiments with a low E:T ratio of 1:25, where the parameter of T cell interaction would be
567 influenced as compared to the standard E:T ratio of 1:3, the following parameters were used:
568 T cell death, organoid contact, speed, square displacement. The reference dataset used to build
569 the global TEG behavior atlas was split into cell tracks to be used as a training dataset (95%)
570 and a test dataset (5%). To reduce dimensionality, for each cell track, four time-series
571 descriptive statistics were quantified and used to train the classifier. For numeric variables, the
572 following measures were computed for each cell track: mean, median, the top 90% of the
573 distribution, and the standard deviation. For binary values, such as the contact with organoids,
574 the mean was calculated, as well as the mean and maximum of cumulative interaction. The
575 random forest classifier was trained using 100 trees on the above-mentioned variables using
576 the nine behavioral signatures as labels (**Figures S2C and S2D**). The test dataset was used to
577 assess for accuracy of the classifier and to determine in which behavioral signatures the errors
578 occurred (**Figure S2E**).
579
580

581 **Correlation between TEG behavior and organoid killing dynamics**

582 To estimate the correlation between the onset of death in individual organoids and the
583 engagement with T cells belonging to the engaging clusters (C7-9), we implemented a
584 technique of sliding window correlation analysis, previously used for functional brain
585 connectivity (Preti et al., 2017) and genome analysis (Burke et al., 2010). We calculated the
586 Pearson correlation coefficient between the cumulative number of organoid contacts with
587 TEGs from each cluster and the increase in dead cell dye intensity in each over a sliding
588 window of 3 hrs (**Figures 2F and S2F**).

589

590 **T cell serial killing capacity analysis**

591 For accurate long-term (up to 24 h) T cell tracking, TEGs were plated at a E:T ratio of 1:25.
592 Tracks were manually corrected where required. Tracks were divided into shorter subtracks of
593 160 minutes. Using the random forest classifier described above, each subtrack was assigned
594 to a behavioral signature (**Figures S2D and S2E**). The following statistics were calculated for
595 each type of behavioral signature (9 clusters): for continuous variables (square displacement;
596 speed, T cell death) the mean, median and standard deviation of the upper quantile were
597 calculated, and for discrete variables (organoid contact and interaction with T cells) the mean,
598 cumulative mean, maximum and cumulative maximum were calculated. Principal component
599 (PC) analysis was used to reduce the dimensionality. The top 5 PCs were used to classify the
600 change in behavioral signature over time (**Figures S3B and S3C**). Equivalent to the approach
601 that was used for the full tracks in **Figure 2B**, we computed a cross-distance matrix based on
602 the multivariate time-series data using the dynamic time warping algorithm and performed k-
603 means clustering in UMAP space. The change in behavioral signatures was represented in a
604 time-series color plot where each row represents one cell track and the color codes for

605 behavioral signature (**Figure S3C)**. The relative proportion of $CD4^+$ and $CD8^+$ TEGs in each
606 cluster was calculated and plotted next to each long-term classification (**Figure S3C**).
607 TEGs that engaged to organoids were back-projected to the imaging dataset and their
608 first and second actions upon organoid engagement were visually analyzed (**Figure 3D**). TEG
609 morphological plasticity was calculated by measuring the cell elongation (ratio between the
610 longest and shortest axes) per cell and per individual timepoint. For each cell track, the
611 plasticity was then computed as the ratio between the maximal and the minimal cell elongation
612 (**Figure S3F**). The actions of $CD4^+$ and $CD8^+$ TEGs upon organoid engagement (**Figure 3D**)
613 as well as the speed of killing and serial killing potential (**Figures 3G and 3H**) were quantified
614 using Imaris software. Only TEGs were included for which tumor cell killing was clearly
615 observed (usually visible as a decrease in living cell dye and an increase in dead cell dye, which
616 co-occurred in many cases with target cell detachment from the organoid). For cases where a
617 single organoid was fully killed by a single TEG, the number of cells killed by the TEG was
618 calculated by dividing the killed volume by the average volume of a single 13T cell (2182
619 μm^3). The killing rate of TEGs was measured as the time period from target cell engagement
620 until tumor cell death (**Figure 3H**).
621
622 **NCAM1 pre-labelling quantification using 3D imaging data**
623 Behavioral classification of NCAM1 pre-labelled TEGs was performed as described above, by
624 predicting behavioral signatures with the Random Forest classifier. $NCAM1^{+/-}$ TEGs were
625 identified based on an NCAM1 intensity threshold in individual TEGs, visually defined at the
626 timepoints where the 488 nm laser was turned on. To ensure inclusion of true $NCAM1^-$ or
627 $NCAM1^+$ TEGs, two intensity thresholds were defined. Only tracks with a defined $NCAM1^+$
628 or $NCAM1^-$ identity were used for subsequent analysis. For each individual well, a difference

629 in percentage of NCAM1^{+} and NCAM1^{-} TEGs was calculated per behavioral signature
630 (**Figures 3L and S3I**).
631
632 **PDO bulk RNA sequencing**
633 For bulk RNA sequencing characterization, RNA of PDOs grown in 'Type 1' culture medium
634 was isolated according to the manufacturer's protocol using the RNeasy Mini Kit (QIAGEN).
635 Quality and quantity of the RNA samples and the libraries were measured with Agilent's
636 Bioanalyzer2100 and Invitrogen™ Qubit™ 3.0 Fluorometer. Quality control was done using
637 FastQC, alignment has been done using STAR
638 (https://github.com/alexdobin/STAR/releases/tag/STAR_2.4.2a) and reads have been mapped
639 to the GRCh37 version of the human reference genome. Quality control on the bams was done
640 using Picard. Read counts were generated with Htseq-count after which normalization is done
641 using DESeq. RPKMs have been calculated with edgeR. For the library preparation the TruSeq
642 Stranded mRNA Library Prep kit from Illumina was used. Sequencing was performed on the
643 nextseq500 sequencer (also Illumina) with single-end 75bp reads. PDO cultures were ranked
644 by responsiveness to TEGs (**Figure 1D**) and differentially expressed genes between the 6 most
645 TEG-sensitive and 6 least TEG-sensitive cultures were analyzed. Genes exhibiting a more than
646 4-fold expression change with an adjusted p-value <0.05 after multiple hypothesis testing
647 correction were used as input gene set enrichment analysis.
648
649 **SORTseq sample preparation**
650 For sequencing of different behavior-enriched TEG populations (**Figure 4A**), TEGs
651 (>0,8x10^{6} per condition) were either (1) co-cultured with 13T PDOs (E:T of 1:3) and separated
652 into organoid-engaged (*engaged*) and organoid non-engaged (*non-engaged*) populations by 2
653 slow-spin (30 rcf) centrifugation steps at 6 h co-culture, (2) co-cultured with 10T or 13T PDOs

654 (E:T of 1: 3) and separated at 4 hrs into organoid-engaged and organoid non-engaged
655 populations by a slow-spin (30 rcf) centrifugation step, co-cultured for another 2h with or
656 without addition of fresh PDOs, again followed 2 slow-spin (30 rcf) centrifugation steps to
657 obtain *non-engaged*^{Enriched} and *super-engaged* TEG populations, or (3) cultured for six hrs
658 without addition of PDOs (*no target control*), using 12-wells culture plates (Thermo Fischer)
659 and 'co-culture medium'. To create single-cell suspensions, conditions containing organoids
660 (all '*engaged'* TEG conditions) were treated with TrypLE for seven minutes at 37°C and
661 washed with adDMEM/F12+++. Cells were then stained in FC buffer (2% FCS in
662 PBS) with anti-CD3-APC conjugated antibodies (1:80; BioLegend) and LIVE/DEAD Fixable
663 Near-IR Dead Cell Stain (1:1000; ThermoFisher) for 30 minutes at 4°C and sorted into 384-
664 wells SORTseq plates using a FACS Aria Cell Sorter (BD Biosciences) and directly stored at
665 -80°C until further processing.
666
667 **SORTseq library preparation and sequencing**
668 All sorted plates were processed according to the CEL-Seq2 protocol with the total
669 transcriptome amplification via poly-A RNA-capture, library preparation, and sequencing into
670 Illumina sequencing libraries as previously described(Muraro et al., 2016). Paired-end
671 sequencing (read1: 30 bp; read2: 120 bp) was used to sequence the prepared libraries using an
672 Illumina NextSeq sequencer.
673
674 **Mapping and quantification of SORTseq data**
675 SORTseq data were mapped and reads were counted, using STAR version 2.6.1a on the
676 Hg38p10 human genome (annotated with GenCode v26). Plate-QC was performed using the
677 Sharq pipeline (Candelli et al., 2018). Percentage of ERCC spike-in reads and mitochondrial
678 mRNA reads versus total read count per cell were applied as QC parameters to identify

679 systemic processing or pipetting errors over the plates. Cells with mitochondrial mRNA reads
680 higher than 15%, ribosomal RNA content higher than 30%, or ERCC reads higher than 25%
681 were excluded from the downstream analysis. Cells with fewer than 650 and higher than 4500
682 genes captured, and genes captured in fewer than 2 cells per plate were also excluded. After
683 the initial QC steps, the ERCC spike-in reads were removed from the final count tables.
684

685 **SORTseq and 10x genomics data integration and TEG subpopulation analysis**

686 For analysis of TEGs not exposed to organoids (**Figures 3I, and S3G and S3H**), 3
687 experimental replicates were used consisting of two datasets processed using SORT-seq and
688 one dataset processed using 10x Genomics Chromium Single Cell 3′ gene-expression kit.
689 SORTseq data was processed as described above. For the 10x dataset, (fresh, not co-cultured)
690 TEGs were viability-enriched via FACS by DAPI staining (1:1000; Thermo Fischer) and
691 loaded according to the standard protocol of the Chromium Single Cell 3′ Kit (v3). All the
692 following steps were performed according to the standard manufacturer's protocol. The library
693 was sequenced on an Illumina Novaseq S1-flowcell and 19,000 reads/cell were collected.
694 Single-cell RNAseq data were mapped, and counts of molecules per barcode were quantified
695 using the cellranger(3.1.0) 10x software package to map sequencing data to the GRCh38(3.0.0)
696 reference transcriptome supplied by 10x. Cells with mitochondrial mRNA reads higher than
697 15% and with fewer than 200 or more than 5000 distinct genes were excluded from the
698 downstream analysis. Data were normalized by sequencing depth, scaled to 10,000 counts, log-
699 transformed, and regressed against the UMI-counts and percentage of mitochondrial mRNA
700 using the ScaleData function of the Seurat package. For integration of the 10x genomics (n =
701 1) and SORTseq (n = 2) datasets, we used previously published Seurat v3 data anchor-based
702 integration(Stuart et al., 2019). Briefly, all three datasets were normalized using SCTtransform
703 (Hafemeister and Satija, 2019) followed by selection of 5000 features for downstream

704 integration. Transfer anchors were then learned and applied for integration of all datasets into
705 a combined dataset. Cell visualization and placement in 2D view was achieved using principal
706 component analysis (PCA) followed by Uniform Manifold Approximation and Projection
707 (UMAP)(McInnes et al.). Shared nearest neighbor graph-based clustering was done using
708 Seurat package's FindNeighbors and FindClusters functions with a resolution of 0.8. For cell
709 type identification marker genes for each cluster were calculated using the FindAllMarkers
710 function and examined to profile marker genes that correspond to known cell types. Additional
711 support for identifying cell subpopulations similitudes was achieved by analyzing the
712 differentially expressed genes with a cell-type annotation tool(Cao et al.). Main marker genes
713 used for TEG subpopulations identification are plotted in **Figure S3H.**
714
715 **Pseudotime Trajectory Inference**
716 Two experimental SORTseq replicates of TEGs co-cultured with 13T PDOs, generated as
717 described above, were used for trajectory interference (**Figure S4B)**. Proliferating T cells were
718 excluded from the analysis since they did not show any dynamic inflammatory genes during
719 the analysis. Afterwards, the gene expression table was log normalized with 10,000 scaling
720 factor. Cell visualization and placement in 2D view was achieved using principal component
721 analysis (PCA) followed by Uniform Manifold Approximation and Projection (UMAP)
722 (McInnes et al., 2020). Shared nearest neighbor graph-based clustering was done using Seurat
723 package's FindNeighbors and FindClusters functions with the resolution of 2. Based on marker
724 gene expression of CD8, CD4 and IL17RB (Terrier et al., 2010), TEGs were sub-clustered into
725 3 subtypes; $IL17RB^{-}CD8^{+eff}$, $IL17RB^{-}CD4^{+eff}$ and $IL17RB^{+}CD4^{+mem}$. Downstream analyses
726 were done on each subset separately and compared with each other where mentioned.
727 RunFastMNN function from SeuratWrappers package was utilized to correct for batch effects
728 between the two SORTseq replicates. Unless specified, batch corrected UMAP values were

729 used for visualization of single cells. We used Monocle3 (Cao et al., 2020) package to infer the
730 pseudotime trajectory and significantly dynamic genes for each T cell subtype. For each cell
731 subtype either *no target control* or *non-engaged*^{Enriched} TEGs were designated as the root of the
732 trajectory. In order to have comparable results from both Seurat and Monocle3 packages, the
733 FastMNN batch corrected UMAP coordinates were imported and used throughout the
734 trajectory analysis in Monocle3. In IL17RB^{-}CD4^{+eff} and IL17RB^{+}CD4^{+mem} subtypes, Monocle
735 identified *no target control* cells as a separate partition. In order to have all cells along with a
736 single pseudotime spectrum (e.g., not having several cells with a same pseudotime value), we
737 added maximum pseudotime values of *no target control* T cells to pseudotime values of
738 remaining cells in that subtype. For all TEG subtypes, significant dynamic genes along with
739 the pseudotime trajectory were calculated and identified using Monocle3's graph_test function
740 using 1e-20 *q* value as the significance cutoff. Afterwards, using k-means clustering and also
741 visual inspection of the genes' behavior over the pseudotime, TEGs were clustered into sub-
742 clusters with similar pattern (CL1-8; **Figure 4G**). The expression profile of the genes along
743 with the pseudotime trajectory was plotted using pheatmap package(Kolde et al.) using row
744 scaled (z-score) expression values. Smoothed gene(s) behavior was calculated and visualized
745 recruiting gam smoothing function in ggplot2 package (Wilkinson, 2011).
746
747 **Behavior signature inference over the pseudotime.**
748 To align the pseudotime inference with the different behavioral signatures that we identified
749 with BEHAV3D, we build a probability map distribution for different behavioral signatures
750 over the pseudotime, based on the fundamental principle of transitivity of probabilistic
751 distribution (**Figure 4F**). We defined three states of cells quantified by different methods:

752 • Behavioral_signatures (B_{sig}): {*Static, Lazy, Medium-scanner, Scanner, Super scanner,*
753 *Tickler, Engager, Super engager*}. Behavioral signatures of cells identified by imaging
754 (**Figure 4B**).
755 • Experimental_engagement_state (Exp_{eng}): {*No target control, Non-engaged, Non-*
756 *engaged*^{enriched}*, Engaged, Super-engaged*}. Cell distribution among different
757 experimental conditions (**Figure 4A**)
758 • UMAP_cluster (U_{cl}): {1…X}. Cell assignment to distinct clusters grouping cells with
759 similar gene expression. Shared nearest neighbor graph-based clustering was repeated
760 several times using Seurat package's FindNeighbors and FindClusters functions with a
761 resolution ranging from 1 to 7.
762 From these three different cell states, the following information was quantified:
763 • p(B_{sig}|Exp_{eng}): For each Experimental_engagement_state we quantified the probability
764 distribution of each Behavioral_signature (**Figure 4F**. This was achieved by
765 reproducing the Experimental_engagement_states *in silico* on our imaging data. These
766 values were calculated separately for $CD4^+$ and $CD8^+$ TEGs.
767 • p(Exp_{eng}|U_{cl}): For each UMAP_cluster, we quantified the probability of each
768 Experimental_engagement_state to belong to this cluster.
769 Given these probabilities, we then quantified for each T cell the probability distribution of each
770 unique Behavioral_signature in each UMAP_cluster, using the equation:
771
772 As a result, each cell was assigned a certain probability distribution for different behavioral
773 signatures. To refine the probability map, the same process was repeated for 7 runs with
774 different cluster sizes and the final probability distributions were averaged per cell. Note that
775 for cells belonging to the *No target control* Experimental_engagement_state, a
776 Behavioral_signature called *No target control* was assumed. The probability distribution along

777 the pseudotime trajectory was plotted using pheatmap package[70] of scaled values for each
778 behavioral signature. Given that the non-engaged behavioral signatures (*Static, Lazy, Slow*
779 *scanner, Medium scanner, Super scanner*) exhibited an identical probability map, their values
780 were plotted together. For visualization purpose, extreme outlier values of skewed distributions
781 were transformed to a maximal cutoff value. Based on the probability distribution of different
782 behavioral signatures, the pseudotime was divided into 4 stages (Baseline (no organoids);
783 Environmental stimuli, Short engagement, Prolonged engagement) for each TEG subtype
784 ($CD8^{+eff}$, $CD4^{+eff}$ and $CD4^{+mem}$).
785

786 **Differential gene expression analysis of TEGs co-cultured with distinct PDO cultures**

787 For comparison of TEGs targeting 10T or 13T PDOs (**Figures 5A-5C**), SORTseq dataset was
788 used including TEGs from distinct Experimental engagement states: *Non-engaged*^{Enriched} and
789 *super engager*. *No target control* TEGs were used as a control group. SORTseq data were
790 mapped and quantified and visualized with UMAP as described above. Differential gene
791 expression analysis was performed with the FindMarkers function from Seurat v3. Common
792 and specific gene sets were filtered and visualized by Venn diagram with the VennDiagram
793 package.
794

795 **Gene set enrichment analysis**

796 The functional enrichment analysis in this study for pathway and biological processes
797 annotations for gene sets of interest was conducted using ToppFun on the ToppGene
798 Suite(Kaimal et al.) (**Figures 1H, S4C, and S5B**). An enrichment score was assigned based on
799 gene enrichment ratio and log p value. For redundant annotations, the annotation with the
800 highest gene enrichment ratio was selected. The pathways and biological processes with
801 highest enrichment for gene set of interest were displayed in RStudio.

802 **Serial killer gene signature analysis**

803 Genes of CL7 (**Figure 4G; Table S4 and S5**) were analysed to identify a unique signature for
804 killer TEGs. 61/83 genes composing this cluster were common to TEGs incubated with 13T
805 and 10T organoids and underwent extensive literature curation to identify genes with a known
806 role in T cell cytotoxicity; T cell biology (not related to cytotoxicity); morphological plasticity
807 or other processes such as GTPase signaling, ribogenesis and transcriptional regulation.
808 Overlapping gene roles were plotted in a Venn diagram with the Venneuler package (**Figure**
809 **4K**).

810

811 **Statistical analysis**

812 Statistical analysis was performed using R or Prism 7 software (GraphPad). Results are
813 represented as mean ± s.e.m. unless indicated otherwise; *n* represents independent biological
814 replicates. Two-tailed unpaired t-tests were performed between two groups, unless indicated
815 otherwise. Pearson correlation was used for paired comparison between three different readouts
816 (IFN-γ production, cell viability and live imaging). For live-cell imaging, the increase in dead
817 cell dye between the first and last time point was used as measure. To compare tumor volume
818 in mice treated with TEGs or TEG001 mock cells, two-way ANOVA with repeated measures
819 was performed. To compare frequencies of different behavioral signatures between PDOs, a
820 Pearson's Chi-squared test was applied. To compare the percentage of dead organoids when
821 TEGs were co-cultured with different PDOs, a one-way ANOVA followed by Bonferroni
822 correction was performed. To estimate the change in correlation between 13T PDO death
823 dynamics and cumulative contact with TEGs for different behavioral signatures, data was fitted
824 to a linear mixed model with experimental replicate as random effect to account for variation
825 between them. For cell type enrichment analysis of TEGs' first and second action after
826 engagement, a hypergeometric test was used (Fisher exact test). For comparisons of

827 percentages of distinct TEG subtypes in the same well ($CD4^+$ vs $CD8^+$ or $NCAM^+$ vs NCAM),
828 for each behavioral signature data were fitted to a linear regression model with each individual
829 replicate set as random effect to account for variation between them. For each fitted model, an
830 analysis of variance was computed with an F-test. For comparison of IFN-β treatment, paired
831 t test was performed.
832
833 **Data availability**
834 RNA sequencing and imaging data is available upon request.
835
836 **Code availability**
837 Upon request.
838
839 **Acknowledgements**
840 We are grateful for the technical support from the Princess Máxima Center for Pediatric
841 Oncology and the Hubrecht Institute and Zeiss for imaging support and collaborations. All the
842 imaging was performed at the Princess Máxima Imaging Center. We thank the Princess
843 Máxima Center Organoid Facility for organoid culture support, the flow cytometry facilities at
844 the Princess Máxima Center and Laboratory of Translational Immunology (University Medical
845 Center Utrecht) for cell sorting, the Princess Máxima Center Single Cell Genomics Facility for
846 help with scRNAseq analysis, Single Cell Discoveries (https://www.scdiscoveries.com) for
847 library preparations, and the Hartwig Medical Foundation
848 (https://www.hartwigmedicalfoundation.nl/) for the sequencing. We also acknowledge the
849 Hubrecht Organoid Technology (HUB) for providing PDOs, QVQ for providing NCAM1
850 nanobodies. We would like to thank Linde Meyaard, Jeffrey Beekman and the $Dream3D^{LAB}$ for
851 providing feedback on the manuscript, and Alberto Miranda-Bedate for pilot PDO sequencing

analysis, Hannah Johnson for the voice over of the video and Anna Allemany for insightful advice for behavioral-transcriptomics inference. This work was financially supported by the Princess Máxima Center for Pediatric Oncology, Grants ZonMW 43400003, VIDI ZonMW 917.11.337, CRUK OPTIMISTICC C10674/A27140 (J.P., H.C), Netherlands Organ-on-Chip Initiative NWO 024.003.001 (J.P., H.C.), KWF Grants UU 2014-6790, UU 2015-7601, and UU 2019-12586 (J.K); Grant UU 2017-11393 (Z.S and J.K). K.K. was the recipient of a VENI grant from the Netherlands Organization for Scientific Research (NWO-ZonMW,016.166.140) and was a long-term fellow of the Human Frontier Science Program Organization (HFSPO, LT771/2015). A.C.R is supported by an ERC-starting grant 2018 project 804412. J.F.D was supported by a Marie Curie Global Fellowship and a VENI grant from the Netherlands Organization for Scientific Research (NWO).

Author contributions

J.F.D grew organoids and performed imaging experiments with assistance from H.G.R., E.J.V. and M.G. M.A. designed and performed the computational analysis. M.A. and J.F.D. analyzed the data. M.B.B. and M.B.R. assisted with imaging data processing. J.F.D., A.K.L.W. and E.K. performed scRNAseq experiments. J.P. and D.F. processed PDO sequencing data. H.C.R.A. performed NCAM1 sorts. F.K. and P.B. analyzed the scRNAseq data. A.C. and E.K. produced TEGs and performed IFN-γ assays. H.G.R., I.J. and A.D.M. performed *in vivo* experiments. A.M.B assisted with computational analysis. R.L.I and M.B.R. made the video. O.K. provided organoid cultures. Y.B.E. and K.K. provided support and developed the co-culture live cell staining protocol that was used and further adapted. J.F.D, M.A. and A.C.R. designed the study and wrote the manuscript with support from A.M.M.E., E.J.W., H.G.S, Z.S., J.K. and H.C. This work was jointly supervised by A.C.R, Z.S, J.K, H.C who share senior authorship.

877 **Declaration of Interests**

878 H.C., Y.B.E. and K.K. are named as inventors on patents or patents pending on Lgr5-stem cell
879 based organoid technology and immune cell organoid co-cultures. For full disclosure of HC:
880 https://www.uu.nl/staff/JCClevers/Additional%20functions. J.F.D. is named as inventor on a
881 patent related to organoid technology. Z. S. and J.K are inventors on different patents with γδ
882 TCR sequences, recognition mechanisms, and isolation strategies. J.K. receives research
883 funding from and is scientific advisor and shareholder of Gadeta (www.gadeta.nl).

884

885 **Figure legends**

886

887 **Figure 1. TEG efficacy across organoids of multiple breast cancer subtypes detected by**
888 **multispectral 3D live imaging and *in vivo* TEG targeting**. (**A**) Schematic representation of
889 co-culture preparation. TEGs were generated by engineering peripheral blood αβ T cells to
890 express a defined Vγ9/Vδ2 TCR via retroviral transduction. TEGs were then co-cultured with
891 patient-derived breast organoids (PDOs). (**B**) Schematic representation of the BEHAV3D
892 platform. Fluorescent dyes were combined to specifically label organoids (yellow), TEGs
893 (blue) and dead cells (red). Co-cultures of organoids and TEGs were imaged in 96-well plates
894 using spectral confocal microscopy in 3D, followed by segmentation and tracking of organoids
895 and T cells, and subsequent behavior classification. TEGs of experimental conditions as
896 indicated were sequenced and pseudotime ordering was used to integrate behavioral data.
897 Identified targets were used to manipulate TEG targeting. (**C**) Representative 3D multispectral
898 images of breast PDO cultures (yellow) that show low (1837M), intermediate (10T) and high
899 (13T) killing by TEGs (blue) at the indicated time points of imaging. Dead cells depicted in
900 red. Scale bars, 100 µm (left two columns) and 30 µm (right two columns). (**D**) Quantification
901 of killing of organoids derived from 14 different BC patients upon 24 hr co-culture with TEGs
902 by 3D live cell imaging. All data were corrected for control LM1 T cell responses. (n = 4
903 independent experiments; mean ± s.e.m.; TNBC = triple negative breast cancer; ER = estrogen
904 receptor; PR = progesterone receptor). (**E**) Representative 3D multispectral images showing
905 automated rendering of single organoids (confetti colors) and T cells (blue) (left image), and
906 an enlarged section showing presence of dead cell dye (red) in a single organoid (transparent
907 purple rendering) and TEGs (transparent blue rendering) at the indicated time of co-culture.
908 Scale bars, 100 µm (left image) and 30 µm (right image). (**F**) Quantification of the percentage
909 of dying single organoids (% of total) over time for each PDO co-cultured with TEGs (n = 4

910 independent experiments; mean ± s.e.m.). (**G**) Quantification of the volume of tumors overtime
911 generated by subcutaneous transplantation of 13T (black lines) or 169M organoids (orange
912 lines). Animals received 2 injections of either TEGs (dashed line) or control TEG011 cells
913 (Control; solid line) at the indicated timepoints. (n ≥5 per condition; mean ± s.e.m.). Statistical
914 analysis was performed by Two-Way ANOVA with repeated measures: 13T-TEG vs 13T-
915 control $p < 0.0001$; 169M-TEG vs 169M-control $p=0.0016$. (**H**) Gene ontology enrichment
916 analysis of differentially expressed genes between the six highest versus six lowest TEG-
917 sensitive organoid cultures from d.
918
919 **Figure 2. TEGs exposed to PDOs display high diversities in their behavior with distinct**
920 **killing potential.** (**A**) Representative image of automated tracking of each TEG (left image;
921 10 hrs tracks are rainbow-colored for time). Tracks were classified according to TEG behavior
922 and back-projected in the image (right image; color-coded by cluster). Scale bars, 50 µm. (**B**)
923 Umap plot showing nine color-coded clusters identified by unbiased multivariate timeseries
924 dynamic time warping analysis. Each data point represents a T cell track of 3.3 hrs. Numbers
925 refer to cluster names presented in (C). (**C**) Heatmap depicting relative values of T cell features
926 indicated for each cluster, named according to their most distinct characteristics. AU: arbitrary
927 units in respect to maximal and minimal values for each feature. (OC, organoid contact; Dis,
928 square displacement; Sp, speed; TI, T cell interactions; CD, cell death) (**D**) 3D-rendered images
929 of 100T (low-targeting; left image) and 13T (high-targeting; right image) organoids (grey) and
930 TEGs with 3.3 hr tracks belonging to *lazy* (green) and *super engager* (red) clusters. Scale bars,
931 20 µm. (**E**) Behavioral cluster distribution of TEGs co-cultured with the indicated PDOs and a
932 normal organoid culture (left plot), in relation to their killing capacity (right bar graph)
933 represented as the percentage of dying organoids (% of total) (n ≥ 3 independent experiments;
934 mean ± s.e.m.). X^2 test; $p = 1.132e-08$. (**F**) Pearson correlation between behavior cluster size

935 and the percentage of dying organoids represented in d. CL9 p=0.00006; CL8 p= 0.009; CL7
936 p=0.006; CL5 p=0.014; CL4 p=0.022; CL2 p=0.0019. (n ≥ 3 independent experiments; mean).
937 (**G**) Change in correlation between 13T organoid death dynamics (measured as increase in dead
938 cell dye) and cumulative contact with TEGs (from cluster (C)7-9). Data is represented as mean
939 correlation per timepoint of all single organoids (n = 4 independent experiments). Linear mixed
940 model fitting with each experimental replicate as a random effect: C9 vs C8 p= 5.19e-06; C9
941 vs C7 p < 2e-16.
942
943 **Figure 3. Unique targeting features of TEGs subpopulations and serial killer potential**.
944 (**A**) Representative 3D-rendered images of $CD4^+$ (blue) and $CD8^+$ (red) TEGs and their full
945 tracks (up to 10 hrs) co-cultured with the 13T organoids (grey surface rendering at t = 0).
946 Overview: Scale bar, 50 µm. Zoomed images: Scale bar, 30 µm (**B**) Relative behavioral cluster
947 distribution of TEGs co-cultured with the indicated PDOs and a normal organoid culture. (**C**)
948 Behavioral cluster size difference (%) between $CD4^+$ and $CD8^+$ TEGs co-cultured with the
949 indicated PDOs and a normal organoid culture calculated from B. (n ≥ 3 independent
950 experiments for each co-culture; mean ± s.e.m.) Linear regression model fitting with each well
951 as a random effect: C9 p=7.52E-06; C8 p=0.0034; C7 p=0.00018; C6 p=0.000023; C5
952 p=0.0062; C4 p=0.01; C3 p= 0.001; C1 p=3.01E-06. (**D**) Quantification of the first action and
953 second action of $CD4^+$ and $CD8^+$ TEGs after they engaged with an organoid. n = 3 replicates.
954 Hypergeometric test was used to analyze cell type enrichment in each category. "Kills multiple
955 cells" p<0.0001; "Kills one cell" p= 0.000015; "No killing" p= 0.0018. (**E**) 3D multispectral
956 images showing a $CD4^+$ TEG (green) that kills a 13T tumor cell (becomes red) in a first
957 organoid (yellow) and a second tumor cell in a neighboring organoid (upper panel), and a $CD8^+$
958 TEG (blue) killing a complete 13T organoid of ~18 cells (yellow becoming red) in 11 hrs
959 (lower panel). Scale bars, 30 µm. (**F**) Processed images of j showing 3D-rendered organoids

960 (grey) at t = 0 and the $CD4^+$ TEG (green) or the $CD8^+$ TEG (blue) with their full track rainbow-
961 colored for time. Scale bars, 10 µm. (**G**) Quantification of the number of cells killed in a
962 sequence by $CD8^+$ TEGs in time. (n = 3 independent experiments). (**H**) Quantification of the
963 time it takes to kill one 13T tumor cell for $CD4^+$ TEGs and $CD8^+$ TEGs (n = 3 independent
964 experiments). (**I**) UMAP embedding showing the expression levels of NCAM1. Color gradient
965 represents the log_2-transformed normalized counts of genes. (**J**) Quantification of the
966 percentage of dying 13T organoids (% of total) at 10 hrs of co-culture with either sorted
967 $NCAM1^-CD8^+$ TEGs or $NCAM1^+CD8^+$ TEGs (n = 5 independent experiments; mean ± s.e.m.).
968 Two-tailed unpaired t test, p= 0.0001036. (**K**) Schematic representation of fluorescent labeling
969 strategy of $CD8^+$ TEGs with NCAM1 nanobody and efluor-450 to image and track NCAM1-
970 positive versus -negative TEGs. (**L**) Behavioral cluster difference (%) between $NCAM1^-CD8^+$
971 TEGs or $NCAM1^+CD8^+$ TEGs co-cultured with 13T organoids. (n = 6 independent
972 experiments; mean ± s.e.m.). Linear regression model fitting with each experimental replicate
973 as a random effect: CL9 p=0.0002; CL8 p=0.07; CL2 p=0.005; CL1 p=0.02. (**M**) 3D-rendered
974 images of 13T organoids (grey) from the same well with NCAM+ 'super-engager' CD8+ TEGs
975 (top image) and NCAM- 'lazy' and 'dying' CD8+ TEGs (bottom image). Scale bars, 10 µm.
976

977 **Figure 4. Behavioral-transcriptomic profiling of TEGs upon PDO exposure, engagement**
978 **and killing.** (**A**) Schematic representation of cell population separation for isolation and
979 sequencing of *super-engaged*, *engaged*, *non-engaged*; *non-engaged*^{Enriched}, and *no target*
980 *control* TEGs. (**B**) Distribution of the 9 behavioral signatures described in **Figures 2B and 2C**
981 of the indicated behavior-enriched TEG populations isolated at 6 hrs of co-culture. (**C-E**)
982 UMAP embedding of pooled scRNAseq profiles showing distribution of, $CD8^{+eff}$, $CD4^{+eff}$,
983 $CD4^{+mem}$ TEGs (C), the 5 behavior-enriched TEG populations described in a (D), and
984 normalized gene expression of IFNG and GZMB (E). Colors represent the log_2-transformed

985 normalized counts of genes. (**F**) Heatmap representing the probability distribution of different
986 behavioral signatures and *no target control* over pseudotime for $CD8^{+eff}$, $CD4^{+eff}$ and $CD4^{+mem}$
987 TEGs. Color represents the scaled probability for each behavioral group. (**G**) Heatmap
988 showing normalized gene expression dynamics of TEGs upon exposure and engagement to
989 13T PDOs. Columns represent T cells ordered in pseudotime, rows represent the expression of
990 genes, grouped based on similarity, resulting in 8 gene clusters (CL). CL1-3 represent gene
991 expression patterns shared among TEG subsets. CL4-8 show different expression dynamics
992 between TEG subsets. Horizontal color-bar (on top) represents the corresponding stage of
993 targeting based on data in f. (**H**) Averaged gene expression over pseudotime for all genes from
994 indicated GO terms for the indicated TEG subtypes. Graph background color-shading represent
995 the corresponding stage of targeting. Line colors indicate GO term. (**I**) Gene-expression dot
996 plot for a curated subset of genes at different stages of targeting. Rows depict genes. Dot color
997 gradient indicates average expression, while size reflects the proportion of cells expressing a
998 particular gene (%). (**J**) Violin plots for different TEG subtypes showing averaged expression
999 of genes related to GO term 'Regulation of cell killing' enriched in CL7 from g. Colors indicate
1000 different stages of targeting. (**K**) Venn diagram depicting common and unique functions from
1001 61 conserved genes composing a (serial) killer gene signature.
1002
1003 **Figure 5. IFN-I signaling in PDOs primes TEG efficacy.** (**A**) Top panel: UMAP embedding
1004 of pooled scRNA-seq profiles from *super-engaged* and *non-engaged*^{Enriched} TEG populations
1005 co-cultured with either 13T or 10T PDOs; and *no target control* T cells. TEGs are colored per
1006 experimental condition. Bottom panel: UMAP plot showing the expression levels of IFNG and
1007 GZMB. Colors represent the log_2-transformed normalized counts of genes. (**B**) Venn diagrams
1008 depicting common and unique genes upregulated in TEGs upon 13T and 10T organoid
1009 exposure (environmental stimuli; top panel) or prolonged engagement (*super engagers*; bottom

1010 panel). (**C**) Heatmap of gene expression for genes involved in functional annotations of interest
1011 ("Response to IFN-I", "Cytokine response"), grouped according to TEG populations. (**D**)
1012 IFNA and IFNB expression in PDOs from the BC panel in **Figure 1D**. (**E-G**) Quantification
1013 of dying single organoids in presence or absence of recombinant IFN-β for the following
1014 conditions: organoids co-cultured with TEGs with direct addition of IFN-β, corrected for
1015 responses of LM1 control T cells (E); organoids pre-incubated with IFN-β for 24 hrs before
1016 co-culture with TEGs, corrected for responses of LM1 control T cells (F), and organoids pre-
1017 incubated with IFN-β for 24 hrs and cultured in absence of TEGs (G). Lines connect
1018 experimental replicates. ($n \geq 3$). Statistical analysis in (F) was performed by paired t test: 34T-
1019 IFN-β vs 34T-control $p < 0.0006$; 27T-IFN-β vs 27T-control $p < 0.0216$; 10T-IFN-β vs 10T-
1020 control $p < 0.0402$.
1021

1022 **References**

1023 Abbas, A., et al. (2020). The activation trajectory of plasmacytoid dendritic cells in vivo during
1024 a viral infection. Nature Immunology *21*, 983–997.

1025 Ali, M., Jones, M.W., Xie, X. et al. (2019). TimeCluster: dimension reduction applied to
1026 temporal data for visual analytics. Vis Comput *35*, 1013–1026.

1027 Asmal, M., Colgan, J., Naef, F., Yu, B., Lee, Y., Magnasco, M., and Luban, J. (2003).
1028 Production of ribosome components in effector CD4+ T cells is accelerated by TCR
1029 stimulation and coordinated by ERK-MAPK. Immunity *19*, 535–548.

1030 Bar-Ephraim, Y.E., Kretzschmar, K., and Clevers, H. (2019). Organoids in immunological
1031 research. Nat Rev Immunol *28*, 514.

1032 Barnes, S.E., Wang, Y., Chen, L., Molinero, L.L., Gajewski, T.F., Evaristo, C., and Alegre,
1033 M.-L. (2015). T cell-NF-κB activation is required for tumor control in vivo. J Immunother
1034 Cancer *3*, 1.

1035 Becht, E., McInnes, L., Healy, J., Dutertre, C.-A., Kwok, I.W.H., Ng, L.G., Ginhoux, F., and
1036 Newell, E.W. (2019). Dimensionality reduction for visualizing single-cell data using UMAP.
1037 Nat. Biotechnol *37*, 34-44.

1038 Benci, J.L., Xu, B., Qiu, Y., Wu, T.J., Dada, H., Twyman-Saint Victor, C., Cucolo, L., Lee,
1039 D.S.M., Pauken, K.E., Huang, A.C., et al. (2016). Tumor Interferon Signaling Regulates a
1040 Multigenic Resistance Program to Immune Checkpoint Blockade. Cell *167*, 1540–1554.e12.

1041 Borden, E.C. (2019). Interferons α and β in cancer: therapeutic opportunities from new insights.
1042 Nat Rev Drug Discov *18*, 219–234.

1043 Boukhaled, G.M., Harding, S., and Brooks, D.G. (2021). Opposing Roles of Type I Interferons
1044 in Cancer Immunity. Annu Rev Pathol *16*, 167–198.

1045 Breiman, L. (2001). Random Forests. Machine Learning *45*, 5–32.

1046 Broutier, L., Andersson-Rolf, A., Hindley, C.J., Boj, S.F., Clevers, H., Koo, B.-K., and Huch,
1047 M. (2016). Culture and establishment of self-renewing human and mouse adult liver and
1048 pancreas 3D organoids and their genetic manipulation. Nat Protoc *11*, 1724–1743.

1049 Burke, M.K., Dunham, J.P., Shahrestani, P., Thornton, K.R., Rose, M.R., Long A.D. (2010)
1050 Genome-wide analysis of a long-term evolution experiment with Drosophila. Nature *467*, 587-
1051 90.

1052 Cai, Y., Hossain, M.J., Hériché, J.-K., Politi, A.Z., Walther, N., Koch, B., Wachsmuth, M.,
1053 Nijmeijer, B., Kueblbeck, M., Martinic-Kavur, M., et al. (2018). Experimental and

1054 computational framework for a dynamic protein atlas of human cell division. Nature *561*, 411–
1055 415.

1056 Candelli, T. et al. (2018) Sharq, a versatile preprocessing and QC pipeline for Single Cell RNA-
1057 seq. BioRxiv 250811

1058 Cao, J., Spielmann, M., Qiu, X. et al. (2019). The single-cell transcriptional landscape of
1059 mammalian organogenesis. Nature *566*, 469-502.

1060 Cao, Y. et al. (2020) SCSA: a cell type annotation tool for single-cell RNA-seq data. Frontiers
1061 in Genetics *11*, 490.

1062 Cattaneo, C.M., Dijkstra, K.K., Fanchi, L.F., Kelderman, S., Kaing, S., van Rooij, N., Van den
1063 Brink, S., Schumacher, T.N., and Voest, E.E. (2020). Tumor organoid-T-cell coculture
1064 systems. Nat Protoc *15*, 15–39.

1065 Cazaux, M., Grandjean, C.L., Lemaître, F., Garcia, Z., Beck, R.J., Milo, I., Postat, J., Beltman,
1066 J.B., Cheadle, E.J., and Bousso, P. (2019). Single-cell imaging of CAR T cell activity in vivo
1067 reveals extensive functional and anatomical heterogeneity. J. Exp. Med. *216*, 1038–1049.

1068 Chen, D.S., and Mellman, I. (2017). Elements of cancer immunity and the cancer-immune set
1069 point. Nature *541*, 321–330.

1070 Collins, S., Wolfraim, L.A., Drake, C.G., Horton, M.R., and Powell, J.D. (2006). Cutting Edge:
1071 TCR-induced NAB2 enhances T cell function by coactivating IL-2 transcription. The Journal
1072 of Immunology *177*, 8301–8305.

1073 Crowther, M.D., et al. (2020). Genome-wide CRISPR-Cas9 screening reveals ubiquitous T cell
1074 cancer targeting via the monomorphic MHC class I-related protein MR1. Nature Immunology
1075 *21*, 178–185.

1076 Dekkers, J.F., et al. (2019). High-resolution 3D imaging of fixed and cleared organoids. Nat
1077 Protoc *14*, 1756–1771.

1078 Dekkers, J.F., et al. (2021). Long-term culture, genetic manipulation and xenotransplantation
1079 of human normal and breast cancer organoids. Nat Protoc *16*, 1936-1965.

1080 Dijkstra K.K. et al. (2018). Generation of Tumor-Reactive T Cells by Co-culture of Peripheral
1081 Blood Lymphocytes and Tumor Organoids. Cell *174*, 1586–1598.e12.

1082 Dunn, G.P., et al. (2005). A critical function for type I interferons in cancer immunoediting.
1083 Nature Immunology *6*, 722–729.

1084 Esteva, F.J., Hubbard-Lucey, V.M., Tang, J., and Pusztai, L. (2019). Immunotherapy and
1085 targeted therapy combinations in metastatic breast cancer. Lancet Oncol. *20*, e175–e186.

1086 Ganesh, K., Wu, C., O'Rourke, K.P., Szeglin, B.C., Zheng, Y., Sauvé, C.-E.G., Adileh, M.,
1087 Wasserman, I., Marco, M.R., Kim, A.S., et al. (2019). A rectal cancer organoid platform to
1088 study individual responses to chemoradiation. Nat. Med. *25*, 1607–1614.

1089 Gründer, C., van Dorp, S., Hol, S., Drent, E., Straetemans, T., Heijhuurs, S., Scholten, K.,
1090 Scheper, W., Sebestyen, Z., Martens, A., et al. (2012). γ9 and δ2CDR3 domains regulate
1091 functional avidity of T cells harboring γ9δ2TCRs. Blood *120*, 5153–5162.

1092 Hafemeister, C., and Satija, R. (2019). Normalization and variance stabilization of single-cell
1093 RNA-seq data using regularized negative binomial regression. Genome Biol. *20*, 296.

1094 Halle, S., Keyser, K.A., Stahl, F.R., Busche, A., Marquardt, A., Zheng, X., Galla, M.,
1095 Heissmeyer, V., Heller, K., Boelter, J., et al. (2016). In Vivo Killing Capacity of Cytotoxic T
1096 Cells Is Limited and Involves Dynamic Interactions and T Cell Cooperativity. Immunity *44*,
1097 233–245.

1098 Jacob, F., Salinas, R.D., Zhang, D.Y., Nguyen, P.T.T., Schnoll, J.G., Wong, S.Z.H., Thokala,
1099 R., Sheikh, S., Saxena, D., Prokop, S., et al. (2020). A Patient-Derived Glioblastoma Organoid
1100 Model and Biobank Recapitulates Inter- and Intra-tumoral Heterogeneity. Cell *180*, 188–
1101 204.e22.

1102 Jacquelot, N., Yamazaki, T., Roberti, M.P., Duong, C.P.M., Andrews, M.C., Verlingue, L.,
1103 Ferrere, G., Becharef, S., Vétizou, M., Daillère, R., et al. (2019). Sustained Type I interferon
1104 signaling as a mechanism of resistance to PD-1 blockade. Cell Res *29*, 846–861.

1105 Johanna, I., Straetemans, T., Heijhuurs, S., Aarts-Riemens, T., Norell, H., Bongiovanni, L., de
1106 Bruin, A., Sebestyen, Z., and Kuball, J. (2019). Evaluating in vivo efficacy - toxicity profile of
1107 TEG001 in humanized mice xenografts against primary human AML disease and healthy
1108 hematopoietic cells. J Immunother Cancer *7*, 69.

1109 June, C.H., and Sadelain, M. (2018). Chimeric Antigen Receptor Therapy. N Engl J Med *379*,
1110 64–73.

1111 Kaimal V, Bardes EE, Tabar SC, Jegga AG, Aronow BJ. (2010). ToppCluster: a multiple gene
1112 list feature analyzer for comparative enrichment clustering and network-based dissection of
1113 biological systems. Nucleic Acids Res, *38* (Web Server issue):W96-W102.

1114 Kierkels, G.J.J., Scheper, W., Meringa, A.D., Johanna, I., Beringer, D.X., Janssen, A.,
1115 Schiffler, M., Aarts-Riemens, T., Kramer, L., Straetemans, T., et al. (2019). Identification of a
1116 tumor-specific allo-HLA-restricted γδTCR. Blood Adv *3*, 2870–2882.

1117 Kolde, R., et al. (2015). Package "pheatmap." Mran.Microsoft.com

1118 Liu, H., Rhodes, M., Wiest, D.L., and Vignali, D.A. (2000). On the dynamics of TCR:CD3
1119 complex cell surface expression and downmodulation. Immunity *13*, 665–675.

1120 Lukonin, I., Serra, D., Meylan, L.C., Volkmann, K., Baaten, J., Zhao, R., Meeusen, S., Colman,
1121 K., Maurer, F., Stadler, M.B., et al. (2020). Phenotypic landscape of intestinal organoid
1122 regeneration. Nature *586*, 275–280.

1123 Marcu-Malina, V., Heijhuurs, S., van Buuren, M., Hartkamp, L., Strand, S., Sebestyen, Z.,
1124 Scholten, K., Martens, A., and Kuball, J. (2011). Redirecting αβ T cells against cancer cells by
1125 transfer of a broadly tumor-reactive γδT-cell receptor. Blood *118*, 50–59.

1126 McInnes, L., Healy, J., Melville J. (2020) Umap: Uniform manifold approximation and
1127 projection for dimension reduction. ArXiv 1802.03426

1128 Muraro, M.J., Dharmadhikari, G., Grün, D., Groen, N., Dielen, T., Jansen, E., van Gurp, L.,
1129 Engelse, M.A., Carlotti, F., de Koning, E.J.P., et al. (2016). A Single-Cell Transcriptome Atlas
1130 of the Human Pancreas. Cell Syst *3*, 385–394.e3.

1131 Neal, J.T., et al. (2018). Organoid Modeling of the Tumor Immune Microenvironment. Cell
1132 *175*, 1972–1988.e16.

1133 Ooft, S.N., Weeber, F., Dijkstra, K.K., McLean, C.M., Kaing, S., van Werkhoven, E., Schipper,
1134 L., Hoes, L., Vis, D.J., van de Haar, J., et al. (2019). Patient-derived organoids can predict
1135 response to chemotherapy in metastatic colorectal cancer patients. Sci Transl Med *11*.

1136 Preti, M.G., Bolton, T., Van De Ville, D., (2017). The dynamic functional connectome: State-
1137 of-the-art and perspectives. Neuroimage, *160*:41-54.

1138 Rigau, M., Ostrouska, S., Fulford, T.S., Johnson, D.N., Woods, K., Ruan, Z., McWilliam,
1139 H.E.G., Hudson, C., Tutuka, C., Wheatley, A.K., et al. (2020). Butyrophilin 2A1 is essential
1140 for phosphoantigen reactivity by γδ T cells. Science *367*.

1141 Rios, A.C., Clevers, H. (2018) Imaging organoids: a bright future ahead. Nat Methods *15*, 24-
1142 26

1143 Sachs, N., et al. (2018). A Living Biobank of Breast Cancer Organoids Captures Disease
1144 Heterogeneity. Cell *172*, 373-368.e10

1145 Schafer, S.T., Paquola, A.C.M., Stern, S., Gosselin, D., Ku, M., Pena, M., Kuret, T.J.M.,
1146 Liyanage, M., Mansour, A.A., Jaeger, B.N., et al. (2019). Pathological priming causes
1147 developmental gene network heterochronicity in autistic subject-derived neurons. Nat
1148 Neurosci *22*, 243–255.

1149 Scheper, W., Gründer, C., Straetemans, T., Sebestyen, Z., and Kuball, J. (2013). Hunting for
1150 clinical translation with innate-like immune cells and their receptors. Leukemia *28*, 1181–1190.

1151 Schnalzger, T.E., de Groot, M.H., Zhang, C., Mosa, M.H., Michels, B.E., Röder, J., Darvishi,
1152 T., Wels, W.S., and Farin, H.F. (2019). 3D model for CAR-mediated cytotoxicity using patient-
1153 derived colorectal cancer organoids. Embo J. *38*, e100928.

1154 Schumacher, T.N., Scheper, W., and Kvistborg, P. (2019). Cancer Neoantigens. Annu Rev
1155 Immunol *37*, 173–200.

1156 Sebestyen, Z., Prinz, I., Déchanet-Merville, J., Silva-Santos, B., and Kuball, J. (2019).
1157 Translating gammadelta (γδ) T cells and their receptors into cancer cell therapies. Nat Rev
1158 Drug Discov *32*, 1–16.

1159 Serra, D., Mayr, U., Boni, A., Lukonin, I., Rempfler, M., Challet Meylan, L., Stadler, M.B.,
1160 Strnad, P., Papasaikas, P., Vischi, D., et al. (2019). Self-organization and symmetry breaking
1161 in intestinal organoid development. Nature *569*, 66–72.

1162 Sistigu, A., Yamazaki, T., Vacchelli, E., Chaba, K., Enot, D.P., Adam, J., Vitale, I., Goubar,
1163 A., Baracco, E.E., Remédios, C., et al. (2014). Cancer cell-autonomous contribution of type I
1164 interferon signaling to the efficacy of chemotherapy. Nat. Med. *20*, 1301–1309.

1165 Straetemans, T., Gründer, C., Heijhuurs, S., Hol, S., Slaper-Cortenbach, I., Bönig, H.,
1166 Sebestyen, Z., and Kuball, J. (2015). Untouched GMP-Ready Purified Engineered Immune
1167 Cells to Treat Cancer. Clin. Cancer Res. *21*, 3957–3968.

1168 Straetemans, T., Kierkels, G.J.J., Doorn, R., Jansen, K., Heijhuurs, S., Santos, Dos, J.M., van
1169 Muyden, A.D.D., Vie, H., Clemenceau, B., Raymakers, R., et al. (2018). GMP-Grade
1170 Manufacturing of T Cells Engineered to Express a Defined γδTCR. Front. Immunol. *9*, 1062.

1171 Stuart, T., Butler, A., Hoffman, P., Hafemeister, C., Papalexi, E., Mauck, W.M., Hao, Y.,
1172 Stoeckius, M., Smibert, P., and Satija, R. (2019). Comprehensive Integration of Single-Cell
1173 Data. Cell *177*, 1888–1902.e21.

1174 Szabo, P.A., Levitin, H.M., Miron, M., Snyder, M.E., Senda, T., Yuan, J., Cheng, Y.L., Bush,
1175 E.C., Dogra, P., Thapa, P., et al. (2019). Single-cell transcriptomics of human T cells reveals
1176 tissue and activation signatures in health and disease. Nat Commun *10*, 4706–4716.

1177 Tan, T.C.J., Knight, J., Sbarrato, T., Dudek, K., Willis, A.E., and Zamoyska, R. (2017).
1178 Suboptimal T-cell receptor signaling compromises protein translation, ribosome biogenesis,
1179 and proliferation of mouse CD8 T cells. Proc. Natl. Acad. Sci. U.S.A. *114*, E6117–E6126.

1180 Terrier, B., Bièche, I., Maisonobe, T., Laurendeau, I., Rosenzwajg, M., Kahn, J.-E., Diemert,
1181 M.-C., Musset, L., Vidaud, M., Sène, D., et al. (2010). Interleukin-25: a cytokine linking
1182 eosinophils and adaptive immunity in Churg-Strauss syndrome. Blood *116*, 4523–4531.

1183 Tiriac, H., Belleau, P., Engle, D.D., Plenker, D., Deschênes, A., Somerville, T.D.D., Froeling,
1184 F.E.M., Burkhart, R.A., Denroche, R.E., Jang, G.-H., et al. (2018). Organoid Profiling
1185 Identifies Common Responders to Chemotherapy in Pancreatic Cancer. Cancer Discov *8*,
1186 1112–1129.

1187 Tuveson, D., Clevers, H. (2019) Cancer modeling meets human organoid technology. Science
1188 *364*, 952-955.

1189 Van Acker, H.H., Capsomidis, A., Smits, E.L., and Van Tendeloo, V.F. (2017). CD56 in the
1190 Immune System: More Than a Marker for Cytotoxicity? Front. Immunol. *8*, 892.

1191 Van der Leun, A.M., Thommen, D.S., and Schumacher, T.N. (2020). CD8+ T cell states in
1192 human cancer: insights from single-cell analysis. Nat. Rev. Cancer *20*, 218–232.

1193 Van Ineveld et al. mLSR-3D and STAPL-3D reveals the spatio-phenotypic patterning of cells
1194 in healthy and tumor tissues. Nat. Biotechnol, *in press*.

1195 Vlachogiannis, G., Hedayat, S., Vatsiou, A., Jamin, Y., Fernández-Mateos, J., Khan, K.,
1196 Lampis, A., Eason, K., Huntingford, I., Burke, R., et al. (2018). Patient-derived organoids
1197 model treatment response of metastatic gastrointestinal cancers. Science *359*, 920–926.

1198 Vyborova, A., et al. (2020). γ9δ2T cell diversity and the receptor interface with tumor cells. J.
1199 Clin. Invest. *130*, 4637-4651

1200 Weigelin, B., et al. (2020) Cancer cell elimination by cytotoxic T cell cooperation and additive
1201 damage. BioRxiv 2020.04.22.054718

1202 Wilkinson, L. (2011). ggplot2: elegant graphics for data analysis by WICKHAM, H.
1203 doi:10.1111/j.1541-0420.2011.01616.x

1204 Yamamoto, T.N., Kishton, R.J., and Restifo, N.P. (2019). Developing neoantigen-targeted T
1205 cell-based treatments for solid tumors. Nat. Med. *25*, 1488–1499.

1206 Yao, Y., Xu, X., Yang, L., Zhu, J., Wan, J., Shen, L., Xia, F., Fu, G., Deng, Y., Pan, M., et al.
1207 (2020). Patient-Derived Organoids Predict Chemoradiation Responses of Locally Advanced
1208 Rectal Cancer. Cell Stem Cell *26*, 17–26.e6.

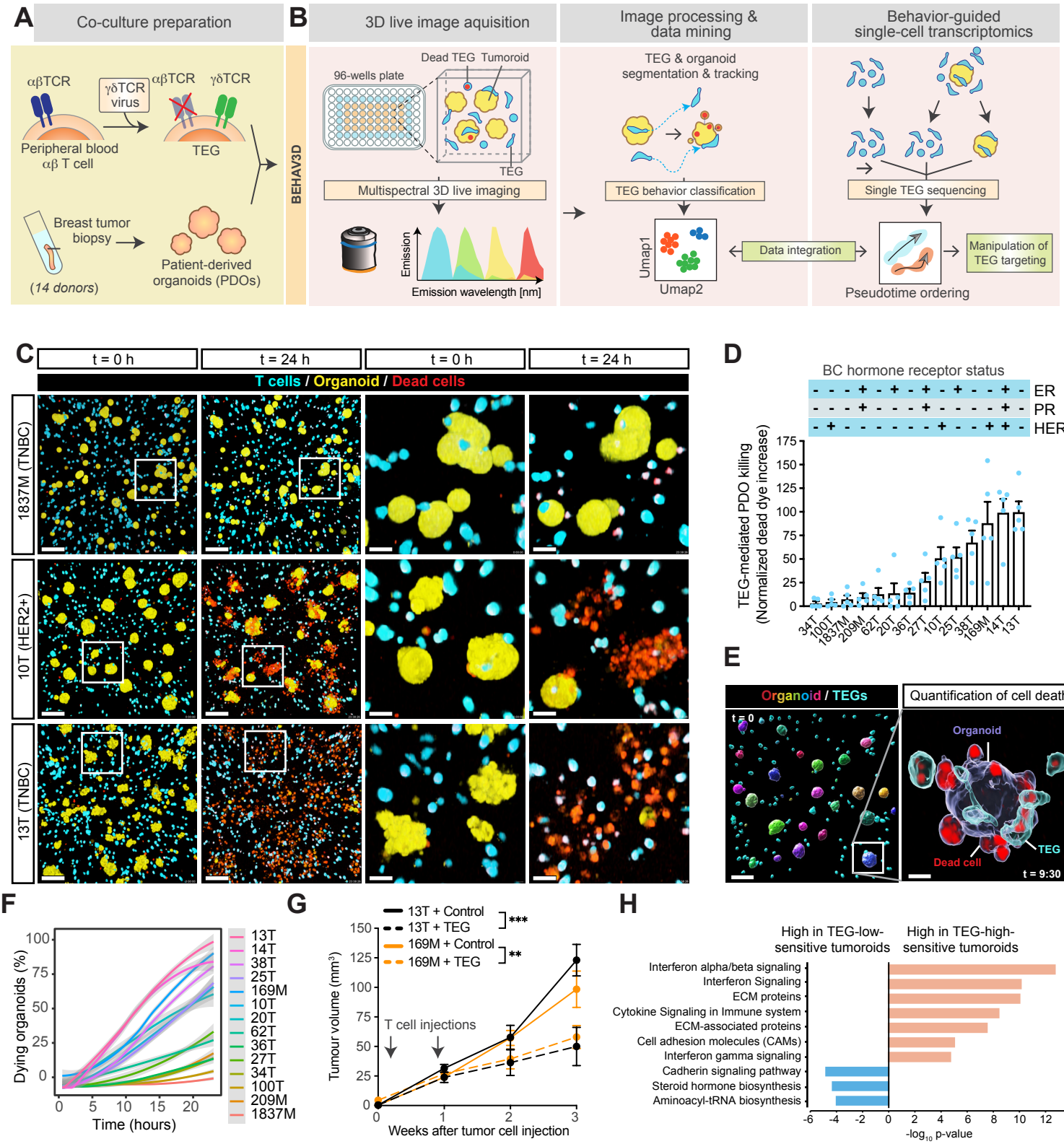
A
Co-culture preparation
αβTCR
γδTCR virus
αβTCR
γδTCR
Peripheral blood αβ T cell
TEG
Breast tumor biopsy
Patient-derived organoids (PDOs)
(14 donors)
B
3D live image aquisition
Image processing & data mining
Behavior-guided single-cell transcriptomics
BEHAV3D
96-wells plate
Dead TEG
Tumoroid
TEG
Multispectral 3D live imaging
Emission
Emission wavelength [nm]
TEG & organoid segmentation & tracking
TEG behavior classification
Umap1
Umap2
Data integration
Single TEG sequencing
Pseudotime ordering
Manipulation of TEG targeting
C
t = 0 h
t = 24 h
t = 0 h
t = 24 h
T cells / Organoid / Dead cells
1837M (TNBC)
10T (HER2+)
13T (TNBC)
D
BC hormone receptor status
ER
PR
HER2
TEG-mediated PDO killing (Normalized dead dye increase)
34T
100T
1837M
209M
62T
20T
36T
27T
10T
25T
38T
169M
14T
13T
E
Organoid / TEGs
Quantification of cell death
t = 0
Organoid
TEG
Dead cell
t = 9:30 h
F
Dying organoids (%)
Time (hours)
13T
14T
38T
25T
169M
10T
20T
62T
36T
27T
34T
100T
209M
1837M
G
13T + Control
13T + TEG
169M + Control
169M + TEG
***
**
T cell injections
Tumour volume (mm³)
Weeks after tumor cell injection
H
High in TEG-low-sensitive tumoroids
High in TEG-high-sensitive tumoroids
Interferon alpha/beta signaling
Interferon Signaling
ECM proteins
Cytokine Signaling in Immune system
ECM-associated proteins
Cell adhesion molecules (CAMs)
Interferon gamma signaling
Cadherin signaling pathway
Steroid hormone biosynthesis
Aminoacyl-tRNA biosynthesis
-log10 p-value

Figure 1

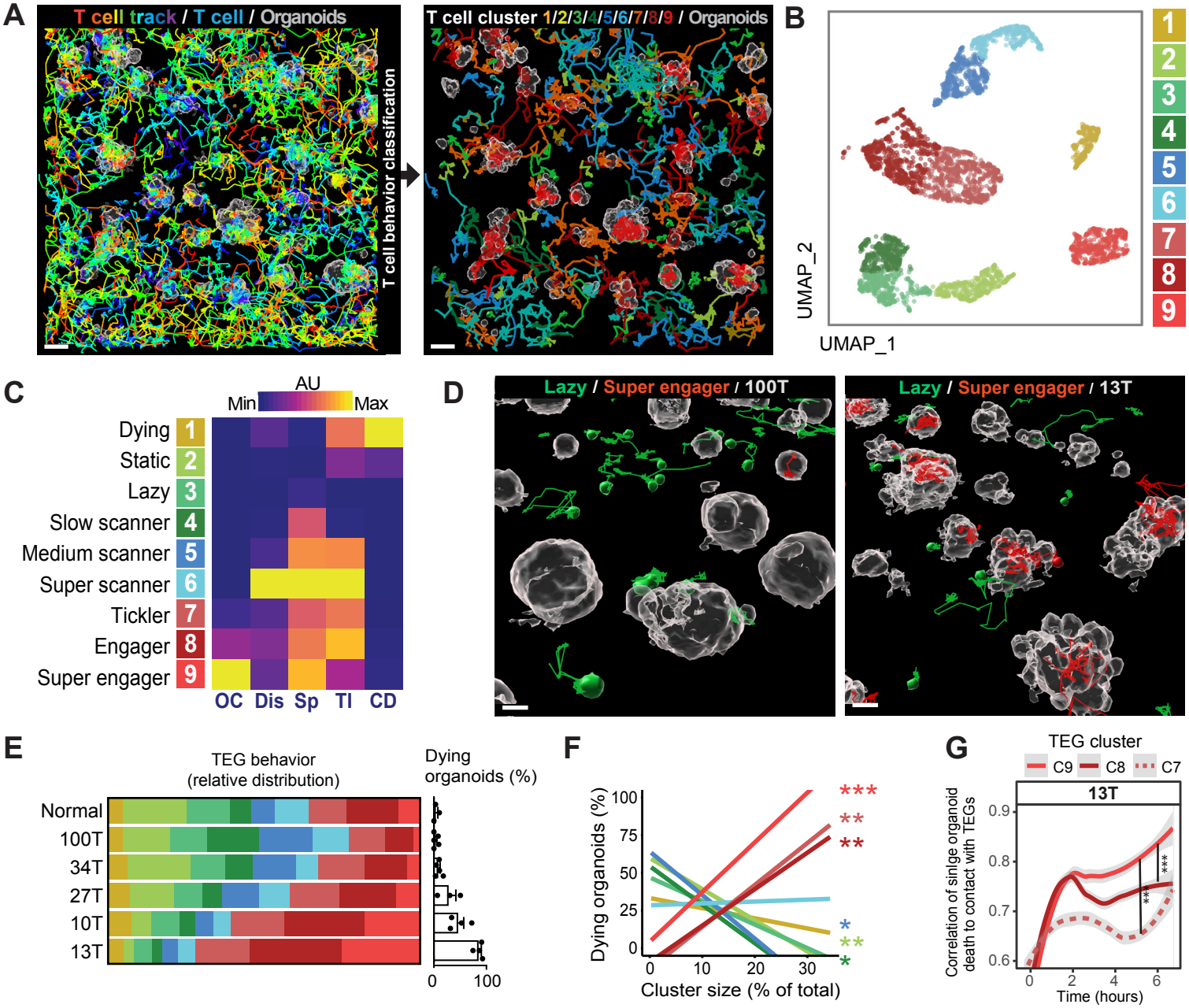
A
T cell track / T cell / Organoids
T cell behavior classification
T cell cluster 1/2/3/4/5/6/7/8/9 / Organoids
B
UMAP_2
UMAP_1
1
2
3
4
5
6
7
8
9
C
AU
Min
Max
Dying 1
Static 2
Lazy 3
Slow scanner 4
Medium scanner 5
Super scanner 6
Tickler 7
Engager 8
Super engager 9
OC Dis Sp Tl CD
D
Lazy / Super engager / 100T
Lazy / Super engager / 13T
E
TEG behavior
(relative distribution)
Dying
organoids (%)
Normal
100T
34T
27T
10T
13T
0
100
F
Dying organoids (%)
100
75
50
25
0
0 10 20 30
Cluster size (% of total)
***
**
**
*
**
*
G
TEG cluster
C9 C8 C7
13T
Correlation of sinlge organoid death to contact with TEGs
0.9
0.8
0.7
0.6
0 2 4 6
Time (hours)
***
***

Figure 2

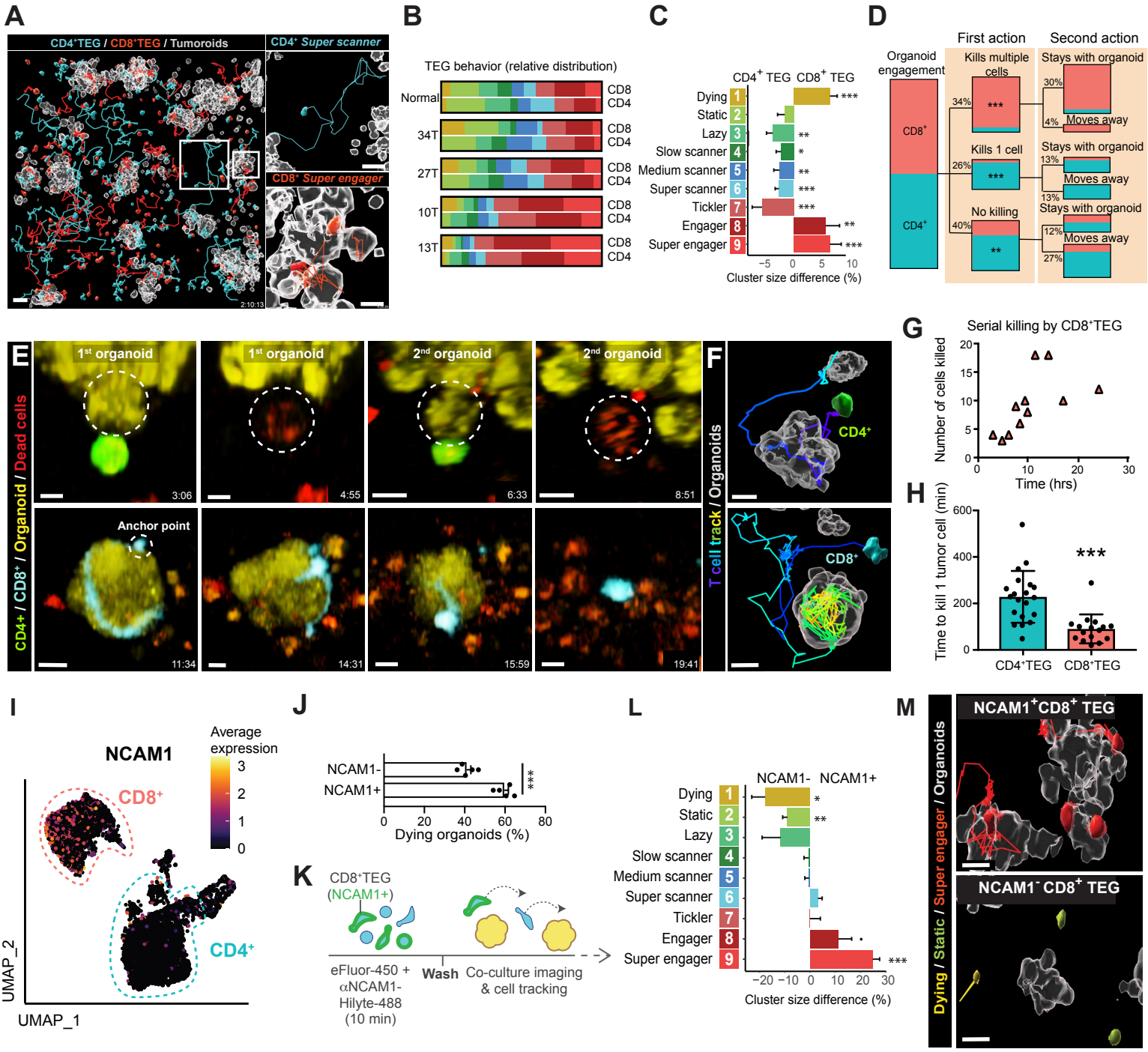
A
CD4+TEG / CD8+TEG / Tumoroids
CD4+ Super scanner
CD8+ Super engager
B
TEG behavior (relative distribution)
Normal
34T
27T
10T
13T
CD8
CD4
C
CD4+ TEG CD8+ TEG
Dying
Static
Lazy
Slow scanner
Medium scanner
Super scanner
Tickler
Engager
Super engager
Cluster size difference (%)
D
First action
Second action
Organoid engagement
CD8+
CD4+
Kills multiple cells
Kills 1 cell
No killing
Stays with organoid
Moves away
E
1st organoid
2nd organoid
Anchor point
CD4+ / CD8+ / Organoid / Dead cells
F
T cell track / Organoids
CD4+
CD8+
G
Serial killing by CD8+TEG
Number of cells killed
Time (hrs)
H
Time to kill 1 tumor cell (min)
CD4+TEG
CD8+TEG
I
NCAM1
Average expression
CD8+
CD4+
UMAP_2
UMAP_1
J
NCAM1-
NCAM1+
Dying organoids (%)
K
CD8+TEG (NCAM1+)
eFluor-450 + αNCAM1-Hilyte-488 (10 min)
Wash
Co-culture imaging & cell tracking
L
NCAM1-
NCAM1+
Cluster size difference (%)
M
NCAM1+CD8+ TEG
NCAM1-CD8+ TEG
Dying / Static / Super engager / Organoids

Figure 3

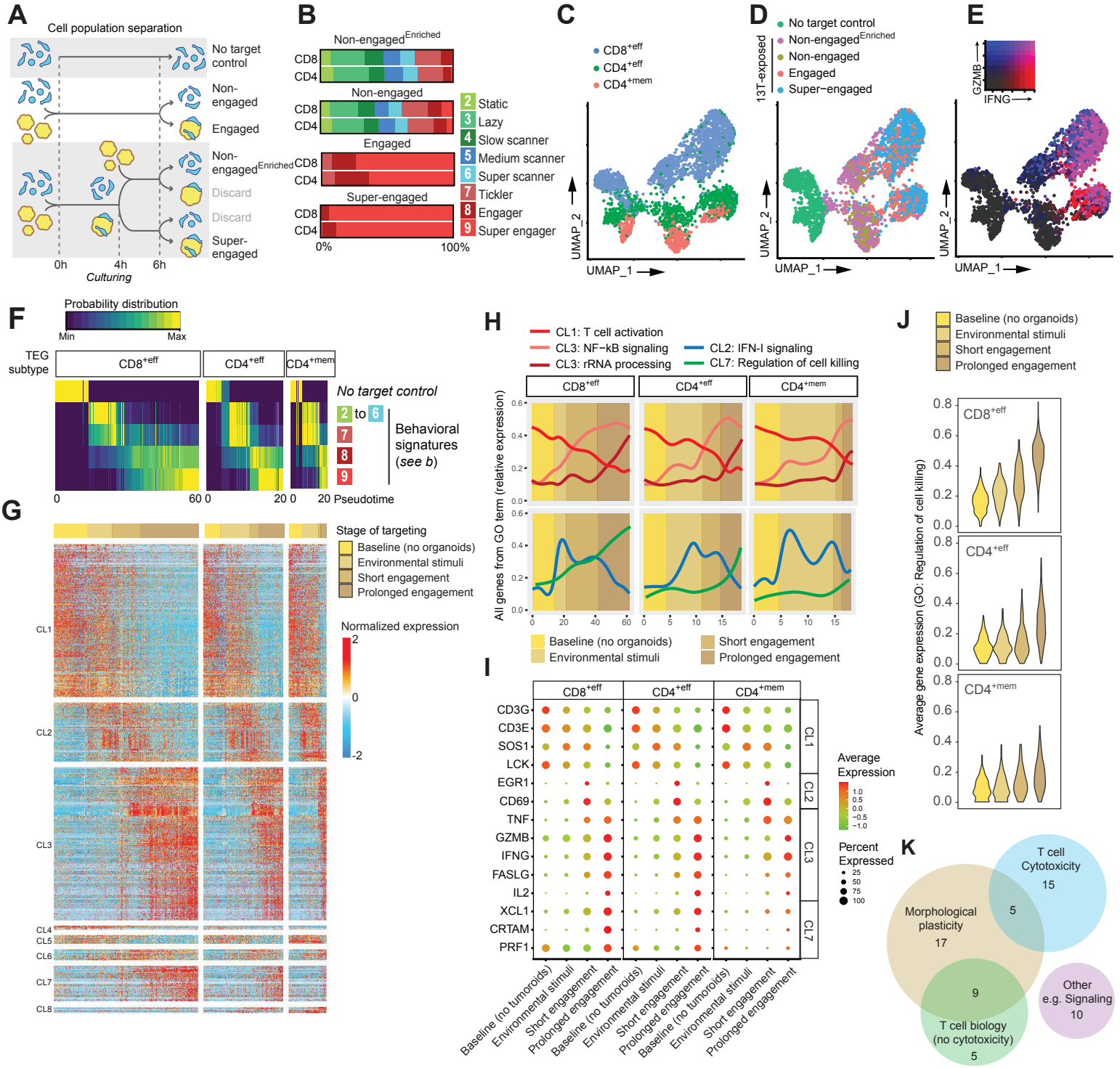
A
Cell population separation
No target control
Non-engaged
Engaged
Non-engaged Enriched
Discard
Discard
Super-engaged
0h
4h
6h
Culturing
B
Non-engaged Enriched
Non-engaged
Engaged
Super-engaged
CD8
CD4
0%
100%
2 Static
3 Lazy
4 Slow scanner
5 Medium scanner
6 Super scanner
7 Tickler
8 Engager
9 Super engager
C
CD8+eff
CD4+eff
CD4+mem
UMAP_1
UMAP_2
D
No target control
Non-engaged Enriched
Non-engaged
Engaged
Super-engaged
13T-exposed
E
GZMB
IFNG
F
Probability distribution
Min
Max
TEG subtype
CD8+eff
CD4+eff
CD4+mem
No target control
2 to 6
7
8
9
Behavioral signatures (see b)
Pseudotime
G
Stage of targeting
Baseline (no organoids)
Environmental stimuli
Short engagement
Prolonged engagement
Normalized expression
CL1
CL2
CL3
CL4
CL5
CL6
CL7
CL8
H
CL1: T cell activation
CL3: NF−kB signaling
CL3: rRNA processing
CL2: IFN-I signaling
CL7: Regulation of cell killing
All genes from GO term (relative expression)
Baseline (no organoids)
Environmental stimuli
Short engagement
Prolonged engagement
I
CD3G
CD3E
SOS1
LCK
EGR1
CD69
TNF
GZMB
IFNG
FASLG
IL2
XCL1
CRTAM
PRF1
Average Expression
Percent Expressed
J
Baseline (no organoids)
Environmental stimuli
Short engagement
Prolonged engagement
Average gene expression (GO: Regulation of cell killing)
K
T cell Cytotoxicity
15
Morphological plasticity
17
5
9
Other e.g. Signaling
10
T cell biology (no cytotoxicity)
5

Figure 4

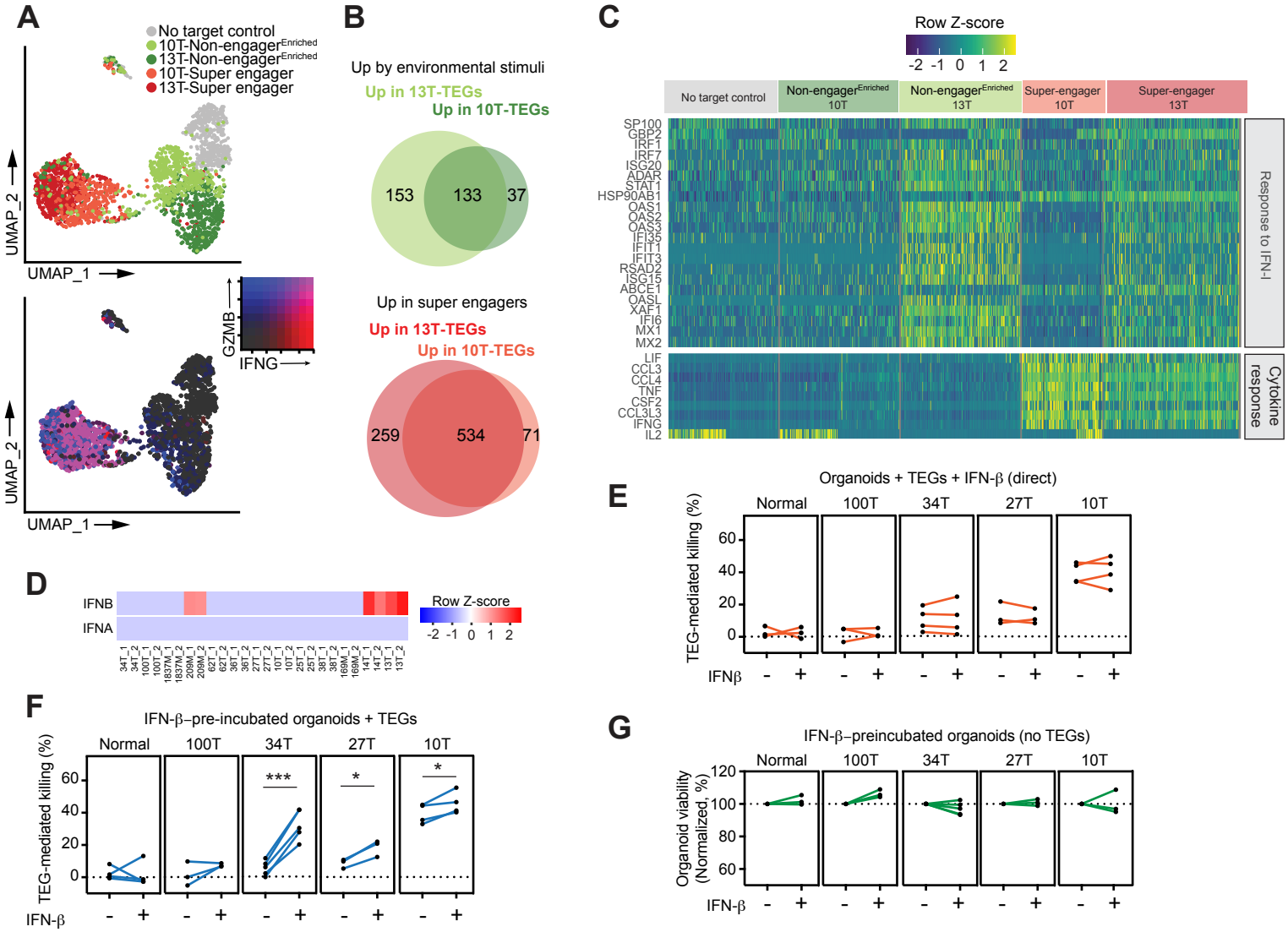
A
No target control
10T-Non-engager Enriched
13T-Non-engager Enriched
10T-Super engager
13T-Super engager
UMAP_2
UMAP_1
GZMB
IFNG
B
Up by environmental stimuli
Up in 13T-TEGs
Up in 10T-TEGs
153
133
37
Up in super engagers
Up in 13T-TEGs
Up in 10T-TEGs
259
534
71
C
Row Z-score
-2 -1 0 1 2
No target control
Non-engager Enriched 10T
Non-engager Enriched 13T
Super-engager 10T
Super-engager 13T
SP100
GBP2
IRF1
IRF7
ISG20
ADAR
STAT1
HSP90AB1
OAS1
OAS2
OAS3
IFI35
IFIT1
IFIT3
RSAD2
ISG15
ABCE1
OASL
XAF1
IFI6
MX1
MX2
LIF
CCL3
CCL4
TNF
CSF2
CCL3L3
IFNG
IL2
Response to IFN-I
Cytokine response
D
IFNB
IFNA
Row Z-score
-2 -1 0 1 2
E
Organoids + TEGs + IFN-β (direct)
Normal
100T
34T
27T
10T
TEG-mediated killing (%)
IFNβ
F
IFN-β–pre-incubated organoids + TEGs
Normal
100T
34T
27T
10T
TEG-mediated killing (%)
***
*
*
IFN-β
G
IFN-β–preincubated organoids (no TEGs)
Normal
100T
34T
27T
10T
Organoid viability (Normalized, %)
IFN-β

Figure 5